Design, Fabrication and Experimental Analysis of Piezoelectric Energy Harvesters with Non-traditional Geometries

By

Lei Wang

A thesis submitted to the

Graduate School - New Brunswick

Rutgers, The State University of New Jersey

in partial fulfillment of the requirements

for the degree of

Master of Science

Graduate Program in Mechanical and Aerospace Engineering

written under the direction of

Professor Kimberly Cook-Chennault

and approved by

_____

_____

_____

New Brunswick, New Jersey

October, 2011

ABSTRACT OF THE THESIS

Design, Fabrication and Experimental Analysis of Piezoelectric Energy Harvesters with Non-traditional Geometries

by Lei Wang

Thesis Director:

Professor Kimberly Cook-Chennault

Unimorph piezoelectric cantilevers with non-traditional surface geometries were investigated by theoretical calculations, finite element models, and sample tests. In this work, we successfully prove that piezoelectric cantilevers subjected to the same load, with the same length and surface area, produce the same the average output voltage regardless of the shape of the surface. Theoretical optimization of the piezoelectric cantilever cross section was also conducted. From this study, we can conclude that piezoelectric devices with trapezoidal-shaped unimorph cross sections can render the maximum average output voltage in comparison to standard rectangular cross sections.

In addition to this work, a novel approach to fabricating thick film dome shaped piezoelectric devices was created. Specifically, several dome-shape piezoelectric devices were fabricated using PZT-epoxy sol-gel and spin coating deposition techniques. The

surface areas of these samples were examined via AFM and SEM. Piezoelectric coefficients, d_{31} and d_{33}, and capacitance were investigated. We were able to demonstrate that the piezoelectric coefficients increased with as the poling voltage was increased.

Acknowledgments

I would like to firstly acknowledge all the assistance from my dear supervisor, Dr. Kimberly Cook- Chennault. With her continuous support for my studies and research, I can go through all the difficulties, no matter from academic field or daily life, and make this thesis possible. Her enthusiasm, inspiration, patience were contagious and motivational for me, from which I also obtain the independent thinking and analyzing abilities. I am so thankful for the profound knowledge, rigorous attitude that she has provided as a successful scientist and professor.

Besides my advisor, I would like to thank all the committee members, Dr. Hae Chang Gea, Dr. Mitch Denda from the Department of Mechanical and Aerospace Engineering, Rutgers University for their encouragement, time, and helpful comments.

The members of the Hybrid Energy System Laboratory have contributed immensely supports in my research and personal life. This lab started from a small group of students without enough lab equipments, and finally became a group of 3 graduate students, several undergraduates and the state-of-art lab facilities. I would like to give my great appreciation to Sankha Banerjee, Sean De Gennaro, Philip Ahn, Nirav Patel, Andrew Tang, Michael, Eric Refour, our summer student from Georgia University, and high school teachers Alan, Robert from RET-E program. I would also like to thank my dear friends in Rutgers, Jian Jiao, Lei Huang, Jia Zhang, Han Sun, Jiandong Meng for making my abroad life less lonely and more fun.

In regards to my experiments, I thank Bob so much for safety and device training in Micro Electronics Research Lab, and his good ideas on sol-gel spin coating. Dr. Warren Lai from Department of Electrical and Computer Engineering is such a nice person, not only answered all my concerns for using lab facilities in MERL, but also acted like my elder family member. I also thank Juan Ren's great help on taking AFM images and inspiration discussions regarding results.

Lastly, I would like to thank my family for all their love and support for my abroad studies. It is hard to spend several years so far away from you, but your love without asking for any return is the true force making me strong. I love you all very much. Thank you.

Lei Wang

Rutgers University

August 2011

Table of Contents

List of Figures

List of Tables

Chapter 1.

Introduction

1.1. Literature Review & Motivation

Piezoelectric materials are ubiquitously used to make devices such as sensors [1-10], actuators [11-16], resonators and filters for telecommunication [17-20], and transducers [21-31]. Recently interest in the field of energy harvesting has burgeoned in both industry and academia due to the desire to produce self-sustainable devices, extend secondary battery life and/or to reduce the mass and size of the overall power supplies of portable electronics. Energy harvesting, or energy scavenging, include mechanisms and processes by which energy is derived from ambient waste energy sources, like vibration, waste heat, solar energy etc. Piezoelectric materials have received attention recently due to their ability to convert mechanical energy directly into electric energy.

1.1.1. Piezoelectric Materials and Piezoelectric Composites

To date a great number of piezoelectric materials have been developed to meet the increasing demand in a variety of applications, e.g. sensors, actuators, hydrophones, transducers, etc. Piezoelectric crystals like Lithium Sulfate and tourmaline are still used in commercial hydrophones [32]; high temperature piezoelectric crystals including Yttrium Calcium Oxyborate $YCa_4O(BO_3)_3$, Lanthanum Gallium Silicate, $La_3Ga_5SiO_{14}$, and Lithium Niobate, $LiNbO_3$, can endure the temperatures up to 1000 ℃, which makes

them suitable in terrestrial environments for applications such as near-engine sensors, ultrasonic drills, corers, and rock abrasion tools [33]. In addition to crystals, the piezo-ceramic is another main category in piezoelectric material family. The most common type of piezo-ceramic used in energy harvesting applications is Lead Zirconate Titanate (PZT). PZT is the solid solution of Lead Zirconate and Lead Titanate. Like many piezoelectric materials, PZT has a perovskite structure, which is any material with the same type of crystal structure as Calcium Titanium Oxide. This type of structure was discovered by Jaffe *et al.* in 1954[34]. Since 1954, the use of piezoelectric materials has increased.

Lead Zirconate Titanate is widely used for the following reasons:

1) It has higher electromechanical coupling coefficients, (~0.6 for PZT-5A, ~0.64 for PZT-5H, and 0.35 for $BaTiO_3$) [35];

2) It can endure higher temperatures for both operation and fabrication (~365 ℃ for PZT-5A and ~193 ℃ for PZT-5H);

3) It can be easily poled;

4) It has a wide range of dielectric constant, (980 for PLZT 8/40/60 and 5700 for PLZT 9/65/35)[36]; and

5) It may be sintered at lower temperatures compared to other common piezo-ceramics such as $BaTiO_3$.

For example PZT ceramics with a bulk density of 7.92 g/cm^3 can be fabricated at a sintering temperature of 1000 ℃ [37], while high density $BaTiO_3$ ceramic materials require sintering at 1200 ℃[38]. Also, PZT can be tailored to achieve optimized properties via addition of different constituent materials [36]. Other than PZT, piezo-

ceramics such as PMN and $BaTiO_3$ have also been studied and applied to actuator, transducer and sensor technologies [36, 39-41].

Despite the popularity of PZT use as transducers, sensors, and energy harvesters; it is inherently brittle. Thus, the amount of strain it can safely absorb without catastrophic failure is limited [1]. To improve performance and address the issue of material brittleness; a great of research has focused on the development of more flexible piezoelectric materials. For example, Polyvinylidene Fluoride (PVDF) is a piezoelectric polymer that has a piezoelectric coefficient of ~6-7 pC/N. Its electromechanical properties are inferior to PZT, which has a piezoelectric coefficient of ~100 pC/N, but PVDF is much more flexible than PZT. For comparison, their properties are provided in Table 1-1 below.

Table 1-1 Comparison of PVDF and PZT properties

	Density (10^3 kg/m^3)	**Relative Permittivity**	**d_{31} Constant (pC/N)**	**g_{31} constant (10E-3 Vm/N)**	**k_{31} constant**	**Acoustic Impedance (10E6 kg/m^2-sec)**
PVDF Film	**1.78**	**12**	**23**	**216**	**12**	**2.7**
PZT	**7.5**	**1200**	**110**	**10**	**30**	**30**

Other than PVDF, piezocomposites have also attracted much attention because the amount and type of constituent materials and fabrication process can be optimized to enhance electrical and mechanical properties based on the requisite application. For example, elastic modulus, electrical impedance, electromechanical coupling, and acoustic impedance are among a few of the properties that can be tailored to meet the need of the application. Also, piezocomposites can be easily formed into complex shapes such as concave and curved structures as opposed to homogenous and single crystal piezoelectric ceramics.

The piezocomposites that incorporate epoxy as binder provide engineers with a wide range of acoustic and mechanical properties. The design and construction of piezoelectric composites was first examined by Newnham and coworkers in 1978. In this work, a way in which the constitutive materials were organized within the connectivity as *connectivity* [29, 42, 43]. The electromechanical properties of composites are governed by the arrangement of phases within the composite, which is referred to as connectivity. The concept of connectivity was first developed by Skinner et al. [44] and later enhanced by Pilgrim et al [45]. In general, 10 connectivity patterns can be used for a diphasic system, which refers to the manner in which individual phases are self-connected. The ten connectivity patterns are (0-0), (0-1), (0-2), (0-3), (1-1), (1-2), (2-2), (1-3), (2-3) and (3-3), where the first digit within the parenthesis refers to the number of dimensions of connectivity for the piezoelectric active phase and the second digit is used for the other phase. All of the ten connective patterns are provided in Figure 1-1. Researchers have shown that composites that with embedded piezo-rods exhibit better properties than the

simpler powder dispersed composites. However, the powder in a matrix approach, which allows for the fabrication of so-called 0-3 connectivity piezocompistes, is still widely studied because the low mass production cost and potential to fabricate to various structures by a coating processes [46]. Another common connectivity pattern; 1-3 connectivity consists of fibers embedded within a matrix and oriented across one dimension of the sample. Different types of connectivity patterns offer different benefits. For example, 3-3 connectivity samples offer electrical paths across the thickness, which enable efficient polarization of ceramic grains. Although the cost for production of 1-3 connectivity samples is more than other types, they have higher electromechanical properties in one direction than other types of piezoelectric composites. 0-3 connectivity samples can be fabricated via relatively simple techniques. This makes them ideal candidates for mass production at a relatively low cost [46].

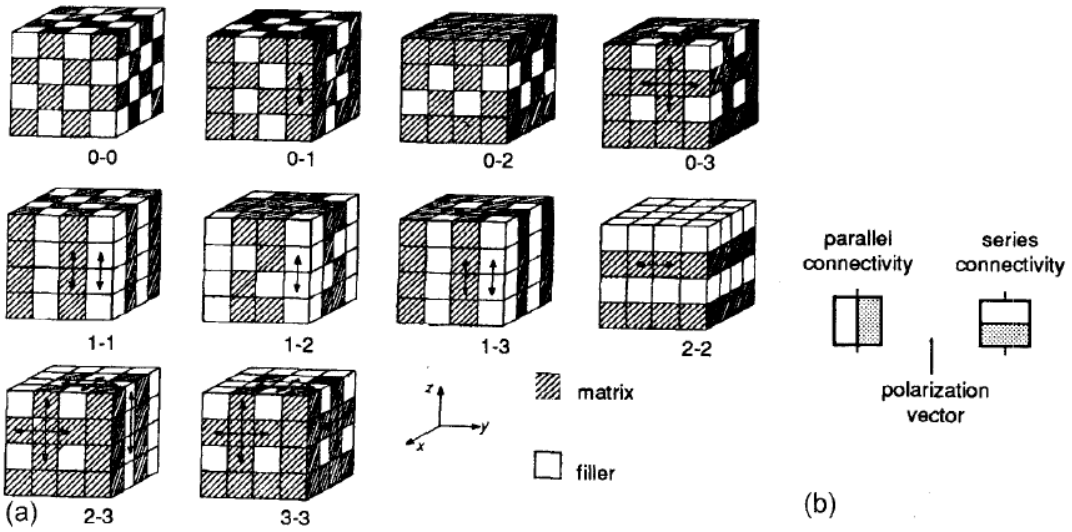

Figure 1.1 (a) Connectivity patterns in a diphasic composite system. (b) Parallel and series connectivities with their respective orientation of the polarization vector. [46]

Many studies have been conducted on 0-3 connectivity piezocomposites. Arlt and Wegener [47] prepared composite films of PZT and PVDF copolymers that were 30 to 150 μm thick. Electron microscopy studies showed that these materials possessed piezoelectric coefficients of up to 22.1 pC/N and 24.8 pC/N for PZT/P(VDF-TrFE) and PZT/P(VDF-HFP) respectively after poling [47]. Liang *et al.* [26, 27] examined a variety of epoxy-piezocomposites ranging from flexible to rigid by making a series of epoxy resins. Banerjee and Cook-Chennault examined the influence of aluminum inclusion size and PZT volume fraction, on the dielectric properties of the three phase PZT-epoxy-aluminum composites and found that addition of Al inclusions enhanced the dielectric and piezoelectric properties [48].

1.1.2. Energy Harvesting using piezoelectric materials

Over the past several decades, the growth of battery technology has helped to advance wireless sensors and wearable electronics to meet growing energy demands. In an effort to extend the battery life and make the portable electronic devices more sustainable, researchers have focused on the development and enhancement of different methods to scavenge energy from the ambient environment, e.g. sun, wind and tide on the macro-scale; and vibration, temperature gradient, human energy on the nano and micro-scale. Roundy [5] undertook a broad survey of potential energy scavenging methods, which is summarized in **Table 1-2**.

Table 1-2 Comparison of energy scavenging and energy storage methods[5]

	Power Density ($\mu W/cm^3$) 1 Year lifetime	Power Density ($\mu W/cm^3$) 10 Year lifetime	Source of information
Solar (Outdoors)	$1.5x10^3$ - direct sun 150 - cloudy day	$1.5x10^3$ - direct sun 150 - cloudy day	Commonly Available
Solar (Indoors)	6 - office desk	6 - office desk	Author's Experiment
Vibrations	200	200	Roundy *et al* 2002
Acoustic Noise	0.003 @ 75 Db 0.96 @ 100 Db	0.003 @ 75 Db 0.96 @ 100 Db	Theory
Daily Temp. Variation	10	10	Theory
Temperature Gradient	15 @ 10 °C gradient	15 @ 10 °C gradient	Stordeur and Stark 1997
Shoe Inserts	330	330	Starner 1996 Shenck & Paradiso 2001
Batteries (non-recharg. Lithium)	45	3.5	Commonly Available
Batteries (rechargeable Lithium)	7	0	Commonly Available
Hydrocarbon fuel (micro heat engine)	333	33	Mehra et. al. 2000
Fuel Cells (methanol)	280	28	Commonly Available
Nuclear Isotopes (uranium)	$6x10^6$	$6x10^5$	Commonly Available

Among the energy scavenging options listed in Table 1-2, piezoelectric devices are being investigated because they directly produce electrical power from application of mechanical static and dynamic loads, which makes it possible to minimize the volume and weight of power supply when they are coupled with other traditional forms of power supplies like batteries. They can also be used to scavenge environmental energy and subsequently charge rechargeable batteries. The efforts of most researchers of piezoelectric energy scavenging devices focus on 1) piezoelectric configurations; 2) implantable and wearable power supplies; 3) ambient fluid flow harvesters; 4) power

harvesting in micro-electromechanical systems; and 5) self-powered sensors [1]. **Table 1-3** summarizes the maximum density for three typically used converters that illustrate that piezoelectric converters have very high practical energy densities.

Table 1-3 Summary of maximum energy density of three types of transducers [5]

Type	Governing Equation	Practical Maximum	Theoretical Maximum
Piezoelectric	$u = \sigma_y^2 k^2 / 2Y$	17.7 mJ/cm^3	335 mJ/cm^3
Electrostatic	$u = \frac{1}{2}\varepsilon E^2$	4 mJ/cm^3	44 mJ/cm^3
Electromagnetic	$u = B^2 / 2\mu_0$	4 mJ/cm^3	400 mJ/cm^3

1.2. Feasibility to utilize energy harvesting techniques with touch and vibration schemes as wearable power supplies

Battery technology has developed over the decades, but their size and mass cannot compete with Moore's Law and the power consumption for wearable electronics. The report of Starner and coworker [49] showed that from 1990 to 2003 the disc storage density has increased over 4000 times; CPU speed, available RAM, wireless transfer speed also increased over 250 times. However the battery energy density has only increased a factor of three during this period, making it the most limiting factor in the design of power supplies for portable electronics with respect to size, weight, and cost.[49]

Anton et al. [1] conducted a review of power supplies for implantable and wearable devices. In their review, they investigated the feasibility of harvesting electrical energy from the human body to power portable electronics via novel structures such as: a spherical shell cap made of piezoelectric material [16], a piezoelectric dome-shaped-diaphragm microgenerator [22], and an initially curved piezoceramic unimorph [50].

Also design studies [7, 51, 52] and optimizations on geometries [2, 13, 53, 54] were examined by many workers whose aim was to increase the energy conversion efficiency, maximize charge generation, induced voltage and output power. Roundy *et al.* [51] concluded that a $1cm^3$ piezoelectric device could generate 375μW from a vibration source of 2.5 m/s^2 at 120HZ [6], to power a radio requiring ~100μWatts that had a data rate of 100 Kbits per second. Otis *et al.* [18] built and tested a micro generator of $1cm^3$ in 2003, which produced 300 μW to power a 1.9GHz radio transmitter when subjected to low-level vibration loading. *Qi et al.* [4] fabricated a prototype generator by printing 500nm thick, 5μm wide piezoelectric ribbons onto rubber for flexible energy conversion. The effective piezoelectric coefficient of their device was 113.7 pm/V after poling. In this study, *Qi et al.* [4] found that they could not move the fully fabricated devices from inorganic substrates to plastic. Compared to PVDF, this novel device had a much higher piezoelectric coefficient (>250 pm/V). Feng [22-24, 55] fabricated a piezoelectric dome-shaped transducer whose energy conversion efficiency was as high as 50% by making a dome-shaped wax mold. Ram and Kiran [16] examined the behavior of a laminated composite spherical shell cap comprised of piezoelectric. Hwan-Sik Yoon *et al.* [50] investigated curved piezoelectric unimorphs, and found that the design parameters for the

curved unimorph subjected to dynamic vibration loading could be optimized to maximize the charge generation. Roundy *et al.* [56] developed a theoretical model for a piezoelectric cantilever with transverse vibration by modeling mechanical and electrical portions of the piezoelectric system as circuit elements. Our work seeks to enhance and expand upon the work of Roundy by conducting a static load analysis of piezoelectric cantilevers.

As discussed earlier, computers are essential to modern life as they are the most frequently used devices, and it has been found that on an average, one adult America uses the computer for ~6 h per every day [57, 58]. Development of reliable energy harvesting devices for portable electronics, like PDA's, cellular phones, and laptops, has attracted much attention from academia and industry [59, 60]. The amount of energy used in key typing motion is simply wasted. Hence one application of the work described here is for powering portable electronics such as these. Wacharasindhu and Kwon [61] designed and fabricated a novel micro-machined energy harvester to harness energy from the typing motion on a computer keyboard. Their design included both electromagnetic and piezoelectric conversion mechanism from typing energy, by assembling a micro spiral coil and a 191 um thick layer of PZT. Experiments showed that the maximum harvested power was about 40.8μW with a 3 mega omega load. **One of our goals is to extend upon this work by examining the feasibility of applying the energy harvesting techniques that we discussed above to key typing in order to scavenge wasted mechanical energy. Here we focus on development of the analytical expressions that can be used to examine the static loading of piezoelectric devices and the**

development of a novel method for fabrication of dome piezoelectric energy harvesting devices.

There are several opportunities for scavenging energy from typing motion, which gives this field of research high prospects. Some of the possible loading scenarios can be on-off push button switches and low frequency typing on keyboards and keypad-based designs. In this work, two main kinds of input mechanism are examined; membrane and dome-switch. These are considered because they are most often found in appliances like mobile phones, pocket calculators, keyboard of laptops. Membrane keyboards usually have a space layer which isolates the front and back layers so they do have an electrical contact, as shown in **Figure 1-2**. When users press the bottom, the finger pushes the front layer down through the isolation space to close the loop. This gives a signal to the keyboard control processor indicating a particular key has been pressed. Dome-switch key boards are a combination of membrane and mechanical keyboards. Users press the front layer to the bottom layer, making a close grid. The difference between the two is the structure using either metal domes or polyester formed domes, like shown in **Figure 1-3**.

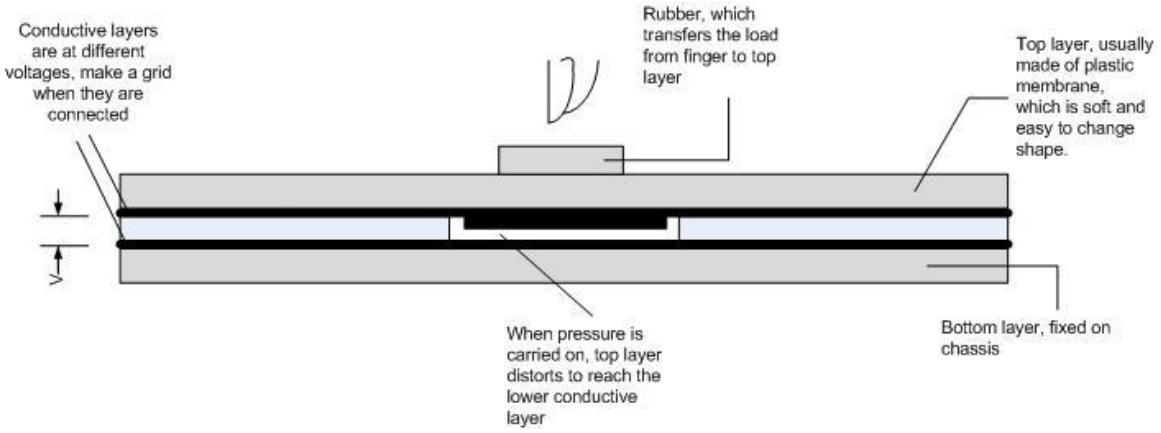

Figure 1.2 Schemes of membrane keyboard mechanism

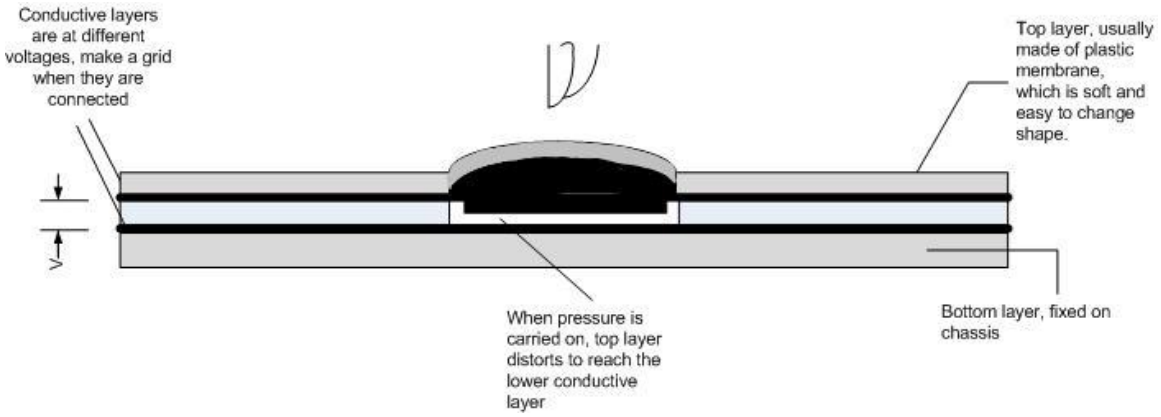

Figure 1.3 Schemes of dome-switch keyboards mechanism

Our idea is to combine the piezoelectric device into the keyboard mechanism so the energy from typing motion may be used to charge secondary batteries of portable electronics. Thus, the realization of this concept hinges on our ability to address the following questions:

1) Piezoelectric cantilevers or beams can be used for membrane keyboards, will geometries of the piezoelectric layer have an effect on output energy?

2) Homogeneous lead zirconate titanate possess extremely large dielectric constants (can be >3000 depending upon orientation and doping) but is very brittle; can piezoelectric composites be used instead of bulk materials?

3) Can novel-shaped piezoelectric devices be economically fabricated for dome-switch keyboards mechanisms?

So far, there has been (to our knowledge) no research conducted on a random shaped cantilever under a static external load, and furthermore there has not been a study on the optimization on the shape of cross section. Hence**,** we have developed an analytical model that allows us to explore the static mode operation of these materials and how geometric parameters affect the average induced voltage. We have conclude this work with the development of a novel method to make piezoelectric energy harvesters that are adaptive to dome-switch keyboards, since fabrication of dome-shape piezoelectric devices is critical for this type of work.

1.3. Research Contributions

The main contribution of this research is the following:

- The analytical study of unimorph piezoelectric cantilevers with random surface geometries, and the FEM analysis for validation of theoretical model.

- An experimental study of trapezoidal, reverse trapezoidal, and hexagon shaped PZT unimorphs.

- Optimization of the shape of cross sections for two configurations of unimorphs.

- Fabrication and test on novel dome-shape piezoelectric devices.

1.4. Overview of the Thesis

The thesis is organized as follows: Chapter 1 reviews the development of piezoelectric materials, energy harvesting technologies using piezoelectric materials, and their applications as wearable power supplies. Chapter 2 deals with the theoretical and FEM analysis of unimorph piezoelectric cantilevers. In Chapter 3 we provide a discussion of the experimental work carried out to validate models in Chapter 2 and gives design rules based on these results. In Chapter 4 we describe the methodology of fabrication of a dome-shaped piezoelectric device and then provide the results from these experiments. Chapter 5 provides a roadmap for future work and next steps.

Chapter 2.

Theoretical and FEM Analysis of Unimorph Piezoelectric Cantilevers with Non-traditional Surface Geometries

2.1. Introduction

Majority of the work in piezoelectric energy harvesting devices has focused on devices comprised of thin rectangular piezoelectric sheets, wherein the profiles of these devices were rectangular. The purpose of this study is to investigate the performance of energy harvesters subjected to static forces. Some researchers have examined the influence of profile shapes on the output power. Roundy, Baker, Dietl *et al.* [51] examined the performance of rectangular, trapezoidal, reverse trapezoidal shaped cantilevers under dynamic loads both analytically and experimentally. Roundy found that a trapezoidal geometry could supply more than twice the specific energy than the rectangular geometry. Baker's experiments showed a 30% higher output power in cantilever beams with the trapezoidal shape, which varied slightly from the theoretical 50% higher power out.[2] Most of these studies focused on small scale piezoelectric devices that scavenge energy from low-level ambient vibration sources, and most of the optimizations on these device geometries focused on trapezoidal and reverse trapezoidal shaped cantilevers subjected to low level-vibrations. However, enhancement of fabrication techniques [4, 62] and demand for minimization of power supplies for portable electronics [63, 64] support the need for further study of different geometrical

shapes subjected to various loading schemes other than vibration, such as static loading modes. The motivations of this work are that there has been little investigation of non-rectangular shaped cantilevers subjected to static external loading, and few studies on the optimization of the piezoelectric device cross section.

In this work, we examine the performance of piezoelectric unimorphs (one piezoelectric layer and one non-piezoelectric layer) under static external load via two types of models. One model consists of a variable shaped surface with a rectangular cross section, as shown in Figure 2.1, another consists a trapezoidal cross section with a rectangular surface. Theoretical results from our first model were validated through FEM models as well as empirical results from experiments. The findings from these studies informed the corresponding design rules we developed. Optimized thickness ratio of both models, and optimized cross sections of the second model were also obtained. This analysis illustrates the feasibility of charging batteries by harvesting energy from keyboard typing.

2.2. Methodology

2.2.1. Analytical model

Model 1: Variable, e.g. surface area that varies as a function of b(x), surface shape with a rectangular cross section

The approach for this analysis is based on Bernoulli-Euler beam theory. In this section, we derive the expression for the average induced voltage and tip displacement for a unimorph subjected to a static load. Two types of unimorph devices are examined: 1) A device with a surface area that varies as a function of b(x) and has a rectangular cross section, and 2) A device with a rectangular surface area and trapezoidal cross section. The first model type is presented in **Figure 2.1.** In **Figure 2.1** an unimorph cantilever device consisting of a non-piezoelectric layer bonded to a piezoelectric layer subjected to a concentrated force, *F*, on its free end, is depicted. The length of the two layers is *L*, while the width in the *x* direction is described by the function, *b(x)*. The two layers are bonded by a conductive adhesive. In our model, the impact of the adhesive thickness and temperature is neglected, because it has been found that the influence of this layer on actuation efficiency is negligible (< ~3%) [65]. The piezoelectric layer is poled along *z* direction, and nickel electrodes are applied on both sides of it for charge collection or voltage measurement. The thicknesses of non-piezoelectric layer and piezoelectric layer are denoted as t_s and t_p respectively. Lead Zirconate Titanate (PZT-5H) is the piezoelectric material and stainless steel is the non-piezoelectric layer.

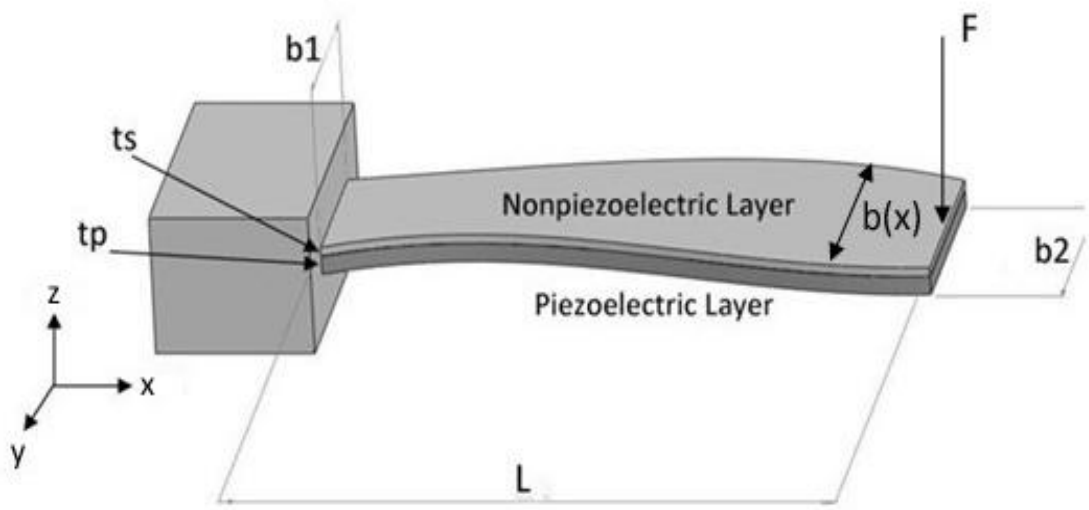

Figure 2.1 A piezoelectric unimorph with a variable surface area and a rectangular cross section.

The constitutive equations for isothermal case can be expressed as

$$\begin{aligned} S_j &= s_{ji}^{E} T_i + d_{jm} E_m \\ D_m &= d_{mj} T_j + \varepsilon_{km}^{T} E_k \end{aligned} \tag{1}$$

where s^E is the compliance tensor at constant electric field, *d* is the piezoelectric coefficient tensor, ε^T is the permittivity matrix at constant stress. In equation (1), the strain, stress and electric displacement are represented by {S}, {T} and {D} respectively.

When we connect the piezoelectric wafer with a voltmeter, the circuit can be generally considered an open circuit, which leads to D = 0, so that

$$E_k = -\frac{d_{mj} T_j}{\varepsilon_{km}^T}, \tag{2}$$

which shows that the electric field is now dependent on stress in an open circuit condition.

A side view of the piezoelectric wafer at any *x*-position with a width of *b(x)* is shown in **Figure 2.2**. When a cantilever is deflected by external force, there will always be a neutral surface at which it is neither compressed nor stretched. Let z-axis along thickness direction (as shown in the diagram), with z=0 at neutral line. The distance from the interface between the stainless steel and PZT layers to neutral line, *a*, can be expressed as the following,

$$a = -\frac{E_s t_s^2 - E_p t_p^2}{2(E_s t_s + E_p t_p)}, \tag{3}$$

where E_s and E_p are Young's modulus for SS and PZT layer respectively.

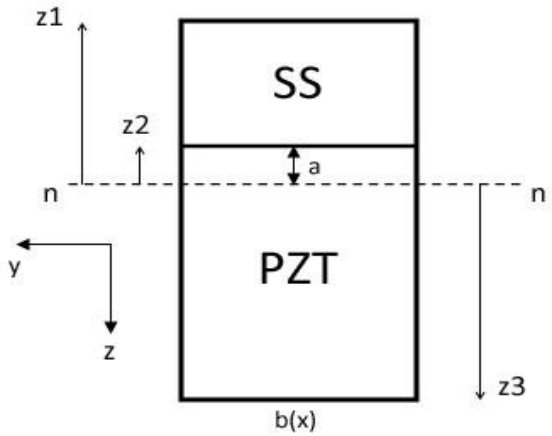

Figure 2.2 Illustration for the rectangular shaped cross section.

Thus the distances from the neutral axis to the top of the SS layer, top of layer *a*, and bottom of the PZT layer can be respectively written as:

$$\begin{aligned} z_1 &= -(t_s + a) \\ z_2 &= -a \\ z_3 &= t_p - a \end{aligned} \quad . \tag{4}$$

The longitudinal stress, σ_{xx}, at a slice surface like **Figure 2.2** can be considered as dependent on strain in *x* direction only, by neglecting the Poisson's effect. Also, the inverse of the radius of curvature can be replaced with the second derivative of deflection, resulting in and expression for the longitudinal stress,

$$\sigma_{xx} = \sigma_k = -E_k z \frac{1}{r} = -E_k z \frac{d^2 w}{dx^2} \quad . \tag{5}$$

In equation (5), the subscript *k* is represented by '*s'* for SS layer and '*p'* for the PZT layers, *r* indicates radius of curvature when cantilever is bent, and *w* is the deflection of a point on neutral line in z-direction for the cantilever.

For any cross section at *x*, the bending moment, *M(x)* is equal to integral of force at every point from z_1 to z_3, that is

$$
\begin{aligned}
M(x) &= \int_{z1}^{z3} \sigma_{xx} z d\mathrm{A} \\
&= \int_{z1}^{z2} -E_s z^2 \frac{d^2 w}{dx^2} \cdot b_x dz + \int_{z2}^{z3} -E_p z \frac{d^2 w}{dx^2} \cdot b_x dz \\
&= -C \cdot b_x \frac{d^2 w}{dx^2}
\end{aligned}
\qquad (6)
$$

where $C = \frac{1}{3}\left[E_s (z_2^3 - z_1^3) + E_p (z_3^3 - z_2^3) \right]$ is considered to be the bending modulus per unit width of the cantilever, and $d\mathrm{A}$ is written as $b_x \cdot dz$.

Meanwhile the bending moment can be defined as

$$
\begin{aligned}
M(x) &= m\ddot{z}\left(L - x\right) \\
&= F(L - x)
\end{aligned}
\qquad (7)
$$

From **(6)** and **(7)**,

$$
\frac{1}{r} = \frac{d^2 w}{dx^2} = -\frac{F(L-x)}{C \cdot b_x} \qquad (8)
$$

Thus **(5)** becomes

$$
\sigma_p = -E_p \frac{z}{r} = \frac{E_p F z (L-x)}{C \cdot b_x} \qquad (9)
$$

This new expression for the stress can be applied to **(2)**, the induced electric field. Since electrodes are applied on both the upper and lower surfaces of the piezoelectric layer; the electric field in the *z*-direction is the only one determined. Thus, the electric field can be represented as,

$$E_3(x,z) = \frac{d_{31}}{\varepsilon_r \varepsilon_0}\sigma_p \tag{10}$$

where ε_r and ε_0 are the dielectric constant of the piezoelectric layer and the permittivity of free space respectively. This expression can be written as a function of the piezoelectric constant, g_{ij},

$$E_3(x,z) = g_{31}\sigma_p, \tag{11}$$

which directly couples the open circuit electric field and applied stress. $E_3(x,z)$ describes the electric field at very point in cantilever.

The average induced electrical potential difference between the two surfaces of the piezoelectric layer can be determined by integrating, $E_3(x,z)$ with respect to z and x, and dividing the result by the thickness and length of the device. Thus, the average induced voltage may be expressed as,

$$\begin{aligned} V_{induce\_ave} &= \frac{1}{A}\int_0^L \int_{z2}^{z3} g_{31}\sigma_p b(x)\,dz\,dx \\ &= k\mathrm{F} \end{aligned} \tag{12}$$

where $k = \frac{1}{4}\frac{g_{31}E_p(z_3^2 - z_2^2)}{AC}L^2$, and A is the surface area of piezoelectric layer.

To calculate the tip displacement of the cantilever, the following boundary conditions are used: axial displacement and its first derivative at the fixed end are equal to zero,

$$w(x=0) = \left.\frac{dw}{dx}\right|_{x=0} = 0 \tag{13}$$

Integrating **(8)** twice results in the following expression for the tip displacement,

$$w = \iint -\frac{F \cdot (L-x)}{C \cdot b_x} dx \tag{14}$$

.

We note that in equation (12) the induced voltage depends linearly on input force at the tip when the parameters t_s, t_p, L and A are fixed. This result is validated by Roundy's work. Specifically, Roundy analyzed the piezoelectric cantilever by modeling both the mechanical and electrical portions of the piezoelectric system as circuit elements [6]. The piezoelectric coupling was modeled as a transformer. The expression that couples the first derivative of induced voltage, *V,* and mechanical strain, δ, was given as following,

$$\dot{V} = \frac{-Ydt_c}{\varepsilon}\dot{\delta} - \frac{1}{RC_p}V \tag{15}$$

where *Y* is the Young's modulus, *d* is the piezoelectric coefficient, t_c represents the thickness of piezoelectric layer, ε is the permittivity, *R* is the resistance of resistive load and C_p is the capacitance of piezoelectric material. The capacitance, C_p is defined as

$$C_p = \varepsilon_r \varepsilon_o \frac{A}{d} . \tag{16}$$

Equations, (15) and (16) illustrate the relationship between induced voltage, *V* and mechanical strain, *δ*, and clearly show that the surface shape of the piezoelectric does not influence induced voltage, which supports our analytical model predictions.

Several researchers have investigated the optimization of the surface shapes for improvement of the energy **conversion efficiency**. Gea *et. al.* [66] used the topology of the piezoelectric device for the design of piezoelectric transducers. In this work, the energy conversion factor,η, was maximized. Gea *et al.* used the following expression for the energy conversion factor,

$$\eta = \frac{\Pi^{E}}{W^{F}},$$

(17)

where W^F represented the work done by the external force and Π^E was the stored electrical energy. The work done by the external force, W^F, was a function of the strain energy, Π^S, and stored electrical energy, Π^E, as shown in equation **(18)**.

$$W^F = \Pi^S + \Pi^E \tag{18}$$

By minimizing $\frac{1}{\eta} = \varsigma = 1 + \frac{\Pi^{S}}{\Pi^{E}}$, the above problem is a standard topology optimization formulation. The optimal configuration was obtained by Gea *et al.* by re-distributing materials among the design domain using a gradient search method. A design comprising of a hollow center and two small supports at each end was proposed as the optimal shape working under an off-plane bending force on the beam tip. The approach

taken in this thesis is significantly different than the novel work of Gea *et. al.* The difference between our works shall be illustrated in the following paragraph.

The work of Gea *et al.* focused on the energy conversion, wherein the ratio of output energy to input energy for devices with different surface shapes was examined. In this work, the work done by an external force, W^F, was a function of the applied force and the displacement, e.g. (Force×Displacement), and the displacement of the device is certainly a function of the surface shape of the device. Hence, this model did not simply consider the input force or displacement solely. **The work in this thesis, along with Roundy's analytical result focus on how much induced voltage can be obtained, but do not include energy input.** For example, with the same force on the cantilever tip, our models will predict an unique induced voltage with various shapes but fixed length and surface area, while Gea's model will have different energy conversion factors (because tip displacement changes with various surface shapes, thus changing the input work). So the influence the surface shape makes is based on the fact that the work done by the applied load is a function of the surface shape, while work (Force×Displacement), is not a parameter studied here.

Model 2: Trapezoidal cross section with rectangular surfaces

Similar to Model 1, we can now examine the effect of shape changes of cross section on the cantilever's performance, while keeping the surfaces rectangular.

Although bulk micro machined 1.5-7 mm thick sol-gel PZT films with rectangular cross sections were recently reported [9, 10], wherein most of piezoelectric wafers were in the order of magnitude of E-4 meter; the difficulties in manufacturing of non-rectangular shaped cross sections on such a thin cantilever makes experimental validation of this model nearly impossible. Thus no experimental validation for Model 2 was performed. Instead, models representing the trapezoidal cross sections are theoretically examined in this section.

In Figure 2.3, a cantilever with a trapezoidal cross section is presented. Two models will be discussed: 1) device where the non-piezoelectric layer is on top of the piezoelectric layer; and 2) device where the piezoelectric layer is on top of the non-piezoelectric layer.

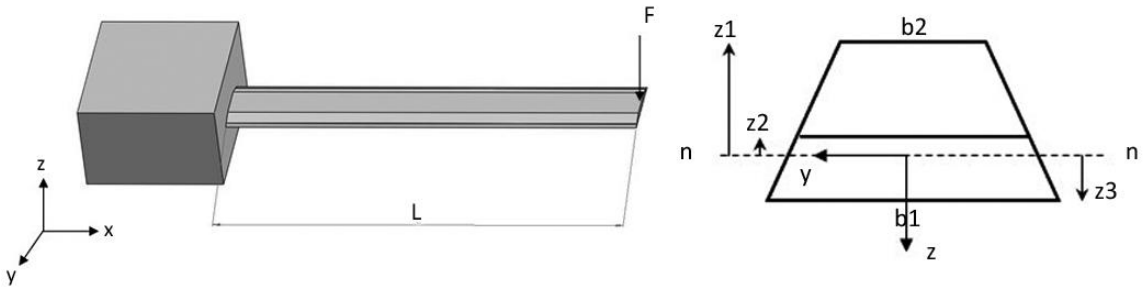

Figure 2.3 A schematic diagram of unimorph cantilever with a trapezoidal shaped cross section. Left: from perspective view; Right: from side view.

First configuration of Model 2: Non-piezoelectric layer above piezoelectric layer

In order to obtain the position of neutral surfaces, notice that when no axial force is applied, the total stress caused by the bending effect at the tip should be zero:

$$\int_{z1}^{z3} \sigma_k dA = 0 \quad , \tag{19}$$

where σ_k is obtained by **(5).**

Assume the width along the *z* direction is *b(z)*, the total height is *h*, so that $dA = b(z) \cdot dz$. Equation **(19)** can then be arranged to be the following:

$$\begin{aligned} &\int_{z1}^{z2} E_s z \frac{d^2 w}{dx^2} \cdot \left[b_2 + \frac{b_1 - b_2}{h} \cdot (t_s + a + z) \right] dz + \\ &\int_{z2}^{z3} E_p z \frac{d^2 w}{dx^2} \cdot \left[b_2 + \frac{b_1 - b_2}{h} \cdot (t_s + a + z) \right] dz = 0 \end{aligned} \tag{20}$$

The expression for *b(z)*:

$$b(z) = b_2 + 2 \tan\theta \cdot (t_s + a)$$

can be used to solve for **(20),** which leads to the position of neutral surface

$$a = \frac{1}{3} \frac{-3E_s t_s^2 b_2 t_p - E_s t_s^3 b_1 - 2E_s t_s^3 b_2 + E_p t_p^3 b_2 + 3E_p t_p^2 b_1 t_s + 2E_p t_p^3 b_1}{2E_s t_s b_2 t_p + E_s t_s^2 b_1 + E_s t_s^2 b_2 + E_p t_p^2 b_2 + 2E_p t_p b_1 t_s + E_p t_p^2 b_1} \tag{21}$$

We can then write the bending moment in the form of $\frac{d^2 w}{dx^2}$ and bending modulus D as in **(6)**,

$$M = -D\frac{d^2w}{dx^2} \tag{22}$$

where

$$D = E_{ss}\left[\frac{A}{3}\left(z_2^3 - z_1^3\right) + \frac{B}{4}(z_2^4 - z_1^4)\right] + E_{pzt}\left[\frac{A}{3}\left(z_3^3 - z_2^3\right) + \frac{B}{4}(z_3^4 - z_2^4)\right]$$

$$A = b_2 + \frac{b_1 - b_2}{h}(t_s + a); B = \frac{b_1 - b_2}{h}$$

Similarly the average induced voltage can be derived as:

$$\begin{aligned} V_{in,ave} &= \frac{1}{L}\int_0^L \int_{z2}^{z3} E_{in}(x,z)dz \cdot dx \\ &= \frac{1}{4}\frac{d_{31}}{\varepsilon_0 \varepsilon_r}\frac{FE_p}{D}(z_3^2 - z_2^2)L \end{aligned} \tag{23}$$

Second Configuration of Model 2: Piezoelectric layer above non-piezoelectric layer

The second configuration for Model 2 is shown as Figure 2.4. The approach in this section is very similar to last one. Some parameters have been changed for the new structure. For this model, the distances from the neutral axis and the bending modulus are defined as

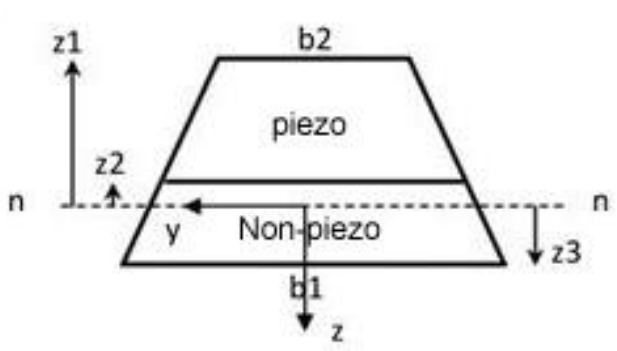

Figure 2.4 Cross section of cantilever with piezoelectric layer above non-piezoelectric layer

$$z_1 = -(t_p + a)$$
$$z_2 = -a$$
$$z_3 = t_s - a$$

$$D = E_{ss}\left[\frac{A}{3}\left(z_3^3 - z_2^3\right) + \frac{B}{4}(z_3^4 - z_2^4)\right] + E_{pzt}\left[\frac{A}{3}\left(z_2^3 - z_1^3\right) + \frac{B}{4}(z_2^4 - z_1^4)\right].$$

The average induced voltage is:

$$V_{in,ave} = \frac{1}{4}\frac{d_{31}}{\varepsilon_0 \varepsilon_r}\frac{FE_p}{D}(z_2^2 - z_1^2)L \tag{24}$$

2.2.2. Finite element model

Finite element models for Models 1 and 2 were created in order to compare the analytical and empirical data (for Model 1). In addition to validation of the analytical model, finite element analysis results are also used to examine the charge distribution and

stress concentrations of the device. The finite element models were created in COMSOL. The material properties for the models are provided in **Table 2-1**.

Table 2-1 Main material characteristics for PZT and SS

	Yong's modulus (GPa)	d_{31} (pm V^{-1})	Relative dielectric constant	Thickness (μm)
PZT	62	-320	3800	127
SS	200			50

The first set of finite element models were created to validate the analytical expressions for Model 1. Here a group of piezoelectric unimorph cantilevers that have the same length and surface area are modeled, with the expectation that the overall induced voltage should be the same, regardless of the surface area geometrical shape. Schematics of the geometries that were investigated are provided in **Figures 2.5 and 2.6**. In **Figure 2.5**, piezoelectric devices that have the same length and surface area are presented. In **Figures 2.6 (d)** and **(e)**, devices with the same surface area, but different lengths are presented. In **figures 2.6 (f)** and **(g)**, devices with the same length, but different surface areas are presented. The dimensions of all of the devices examined are listed in **Table 2-2**.

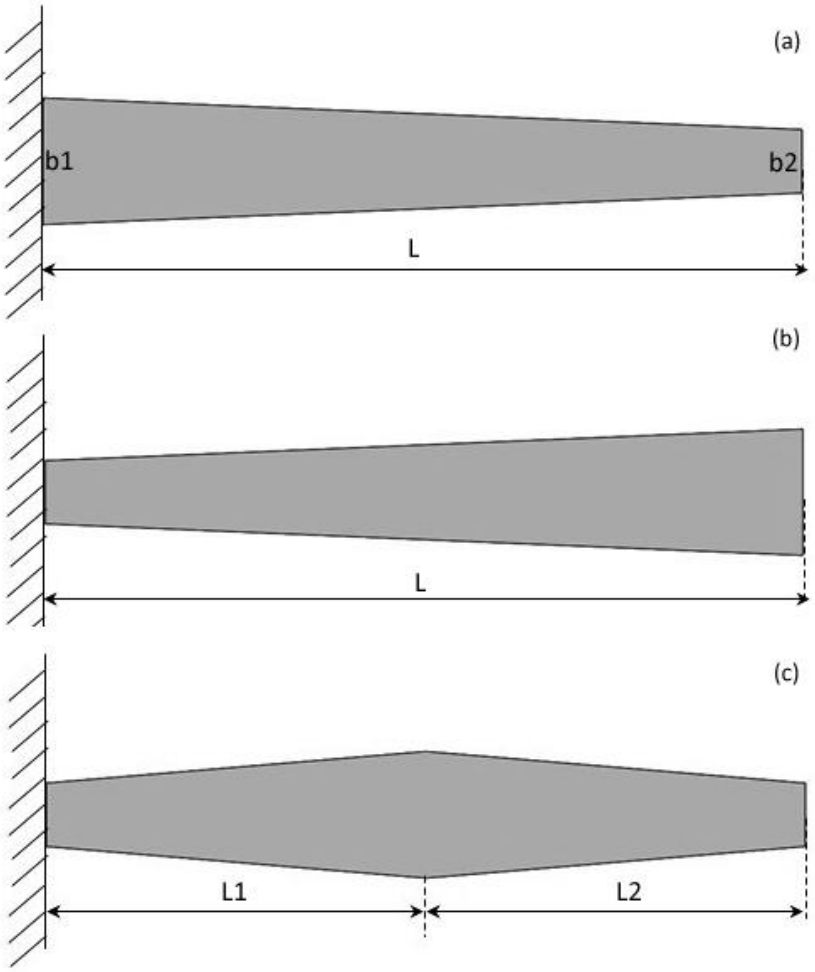

Figure 2.5 A schematic diagram from top view of three piezoelectric unimorph cantilevers with same length and surface area. (a) shows a trapezoidal shape with width b1 on the left end and b2 on the right, while (b) shows a reverse trapezoidal shape. (c) has a hexagon shape consisting of two trapezoidal parts.

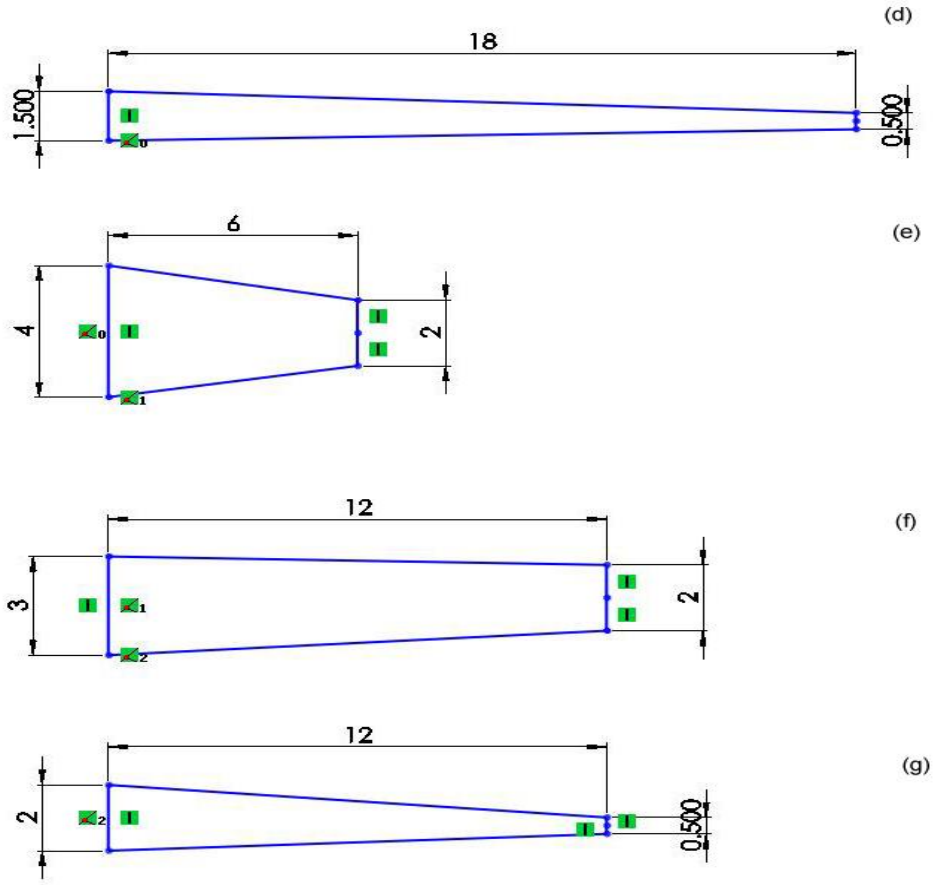

Figure 2.6 A schematic diagram showing four trapezoidal shape cantilevers with either same surface area or same length with ones in Figure 2.4. (d) gives a longer cantilever with same surface area; (e) gives shorter one with same surface area; (f) gives larger area with same length; (g) gives smaller area with same length.

Table 2-2 Dimensions of three models used in FEM validation

Model No.	Length (mm)	Left width b_1 (mm)	Right width b_2 (mm)	Surface Area A (mm^2)
(a)	12.0	2.0	1.0	18.0
(b)	12.0	1.0	2.0	18.0
(c)	6.0/6.0	1.0	1.0	18.0
(d)	18.0	1.5	0.5	18.0
(e)	6.0	4.0	2.0	18.0

(f)	12.0	3.0	2.0	30.0
(g)	12.0	2.0	0.5	15.0

In the models, an induced voltage distribution is generated when a force is applied on the tip of the cantilever. In **Figure 2.7**, the voltage distributions from the bottom of cantilevers with geometries of (a) (b) (c) from Figure 4 are presented. **Figure 2.8** shows the voltage distribution of the rest. A concentrated force of 1N is applied in the middle of the tip, while the nodes at the opposing end are fixed. In order to illustrate the distribution on bottom surface, the direction of z is changed in **Figure 2.7** and **2.8**.

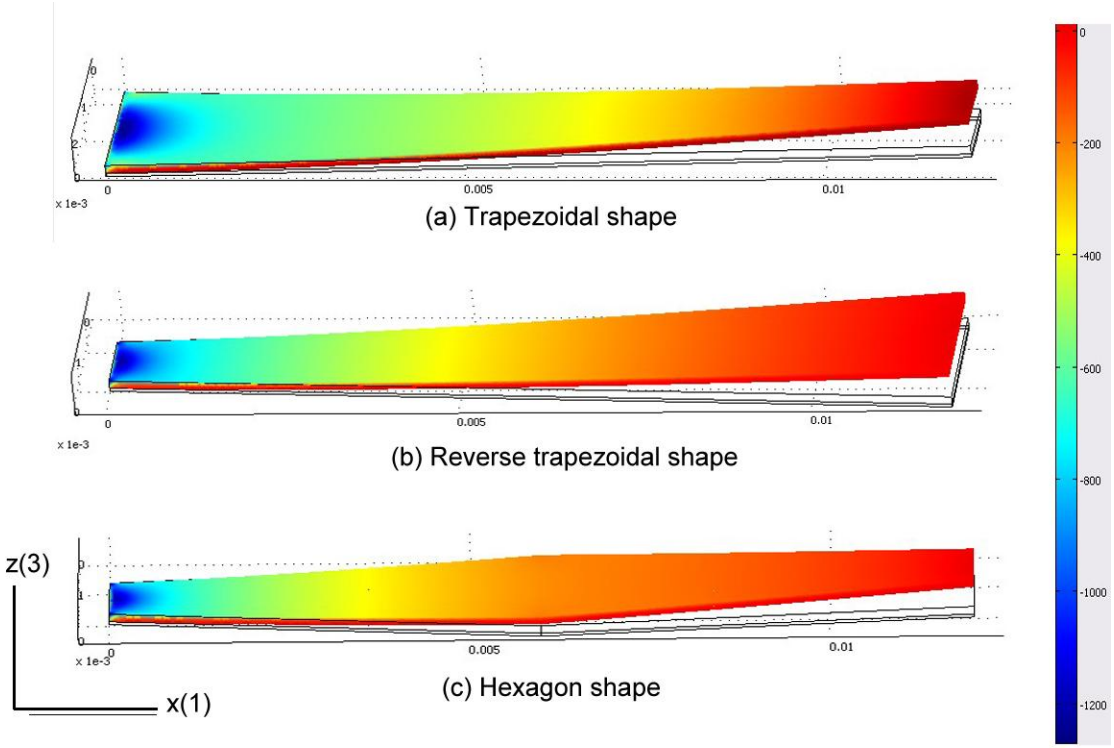

Figure 2.7 Voltage distribution on bottom sides of (a), (b), (c) from FEM analysis

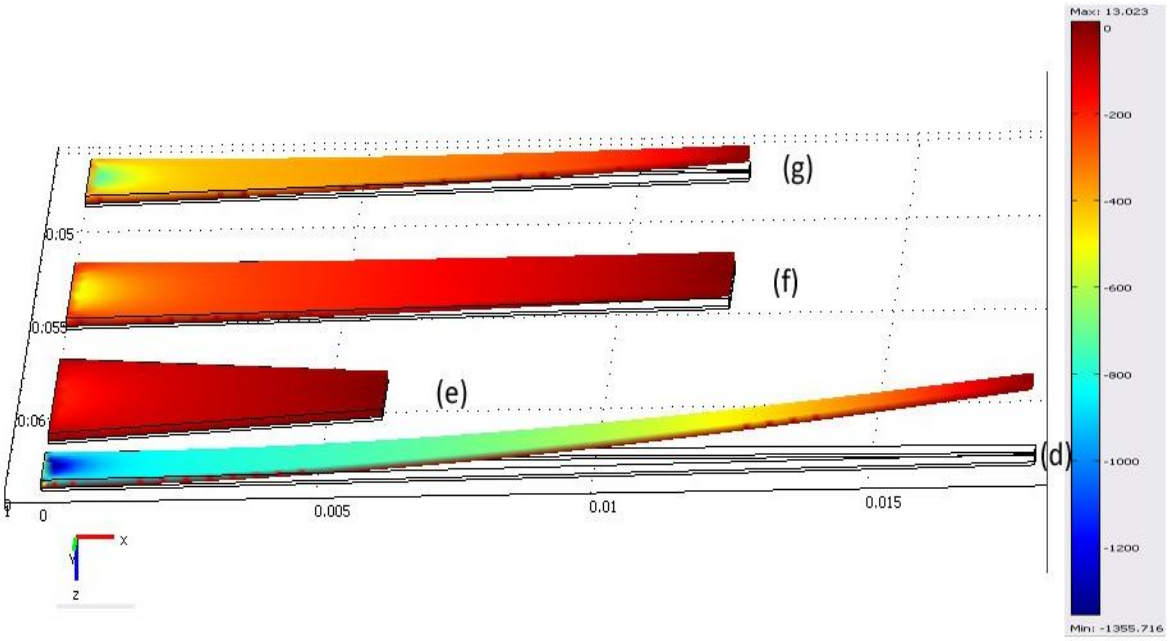

Figure 2.8 Voltage distribution on bottom sides of (d), (e), (f), (g) from FEM analysis

The average induced voltage is obtained by a built-in boundary integration function in COMSOL.

2.2.3. Comparison between models

Results are summarized in **Table 2-3** and plotted in **Fig 2.9**, **Fig 2.10** and **Fig 2.11**.

Table 2-3 Comparison of effective spring constant, average induced voltage upon displacement and unit force for cantilevers with various geometric parameters.

	Effective spring constant(N m^{-1})		Average Induced Voltage per unit tip displacement (mV μ m^{-1})		Average Induced Voltage per unit force (V N^{-1})	
	FEM	Theo.	FEM	Theo.	FEM	Theo.
(a)	158.7	141.3	43.4	44.4	-308.2	-314.4

(b)	111.1	100.1	30	31.5	-300.0	-314.4
(c)	128.2	113.06	38.9	35.6	-299.4	-314.4
(d)	32.6	29.5	21.6	19.9	-660.4	-677.1
(e)	2674.9	2261.3	220.1	170.1	-82.3	-75.2
(f)	256.4	224.0	47.3	40.4	-184.5	-180.5
(g)	143.0	127.7	51.5	46.1	-359.8	-361.1

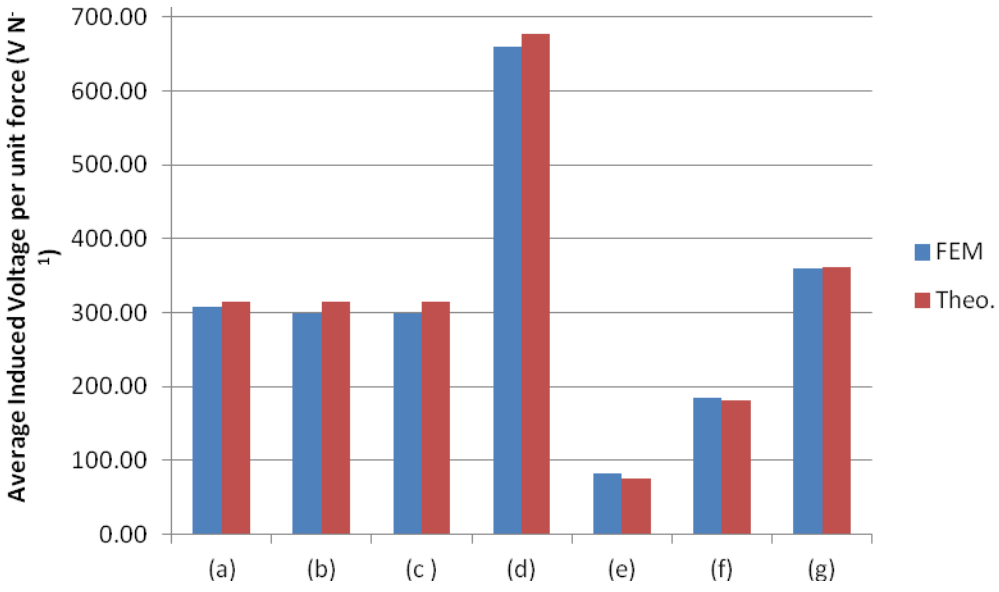

Figure 2.9 Comparison of FEM and theoretical results on average induced voltage per unit force for cantilevers with various geometries.

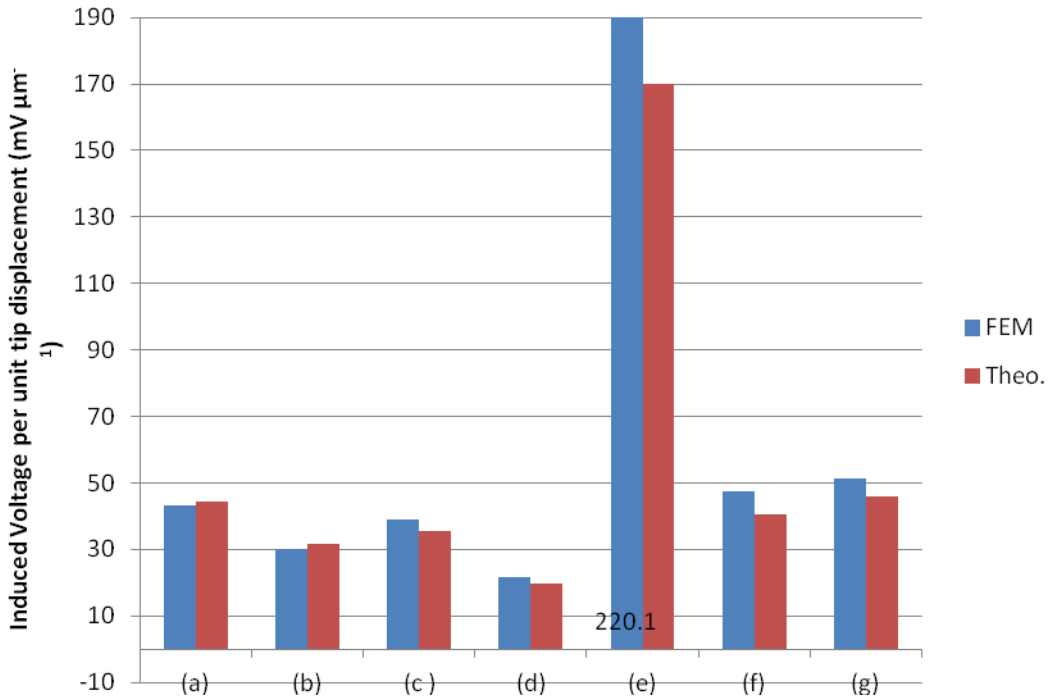

Figure 2.10 Comparison of FEM and theoretical results on average induced voltage per tip displacement for cantilevers with various geometries.

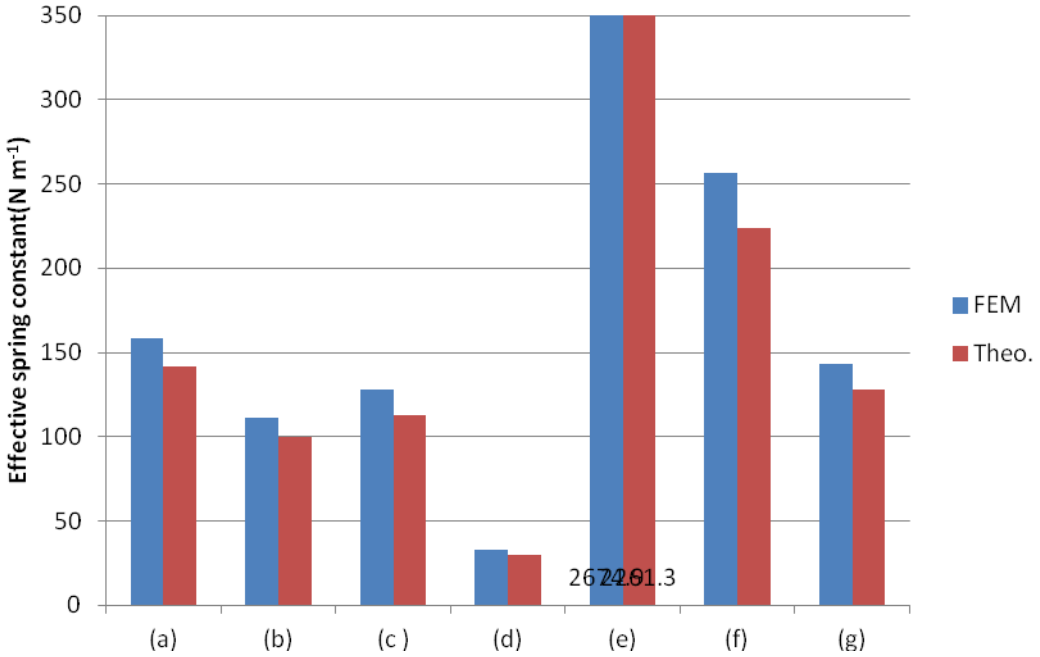

Figure 2.11 Comparison of FEM and theoretical results on effective spring constant for cantilevers with various geometries

As can be seen from the figures above, the results: average induced voltage, induced voltage per tip displacement, and effective spring constant between FEM solution and theoretical analysis are very close. Thus, our analytical models are verified. The in-depth explanation will be provided in discussion, Section 2.4.

2.3. Optimization

2.3.1. Optimal Thickness Ratio for Model 1

The thickness ratio of the SS layer and PZT layer was examined for optimal induced voltage in research by Xiaotong Gao *et al.* [67] Their work showed that an excessively thin SS layer could result in a neutral plane located inside of PZT layer, making PZT layer stretched and compressed on different sides of the neutral plane. They explained that this scenario would result in charge cancellation, and ultimately reduce the overall induced voltage. While on the other hand, a thick SS layer could result in a higher bending modulus, which would cause the induced voltage to be reduced. Similar to Xiaotong's method, we have fixed all of the parameters except for the thicknesses. The following objective function was used in MATLAB

$$\min \quad f(x_1, x_2) = -\left|V_{in,ave}\right|, \tag{25}$$

where x_1 is the thickness of SS layer, and x_2 is the thickness of the PZT layer. We found the optimal SS to PZT thickness layer ratio to be 0.29, where the thicknesses of the layers were 37μm and 127μm for the SS and PZT layers respectively, which is very close to

Xiaotong's 0.28 optimal ratio. Thus, in our work we used a thickness equal to 127μm for the PZT sheets and the SS layers has a thickness of ~37μm.

2.3.2. Optimization for Model 2

The thickness and top width of PZT layer were held constant for the first configuration of Model 2 where, t_p = 127 μm and w_1 = 2mm. In **Figure 2.12** the influence of the width of the upper surface, w_2, on the average induced voltage is depicted, wherein five sets of SS layer thickness are compared. In this figure, the red solid line represents the optimal thickness of stainless steel, with a 127μm thick PZT layer. The diagram shows that for each set of thickness, increasing the upper surface width, results in a drop of output voltage up to certain point, and then an increase slowly at the later part. This actually gives the optimal point for each thickness. When picking a point at low w_2 region (<0.5mm), we see output voltage soars with respect to decrease of thickness of SS layer. Now it is reasonable to think about reducing both w_2 and t_s to see would there be any extreme point for the first configuration. Notice in **Figure 2.12** that some lines start with positive values, and then decrease as the upper surface width increases, and then finally become negative. The positive-negative transition is caused by the shifting of neutral plain. At b_2 = 0, the cross section has a triangular shape, where the neutral plain is very close to the base of triangle. A small distance between the neutral line and base means most of the area at the cross section is under tension, and only a small amount of area is under compression, which ultimately results in a positive voltage. By increasing the upper surface width, the spacing between the neutral line and the base

also increases, which makes less piezoelectric cross section area under tension and more under compression. At the extreme situation, cross section area under tension and compression are exactly the same, and thus there is a zero voltage output, because the positive and negative voltages simply cancel with each other.

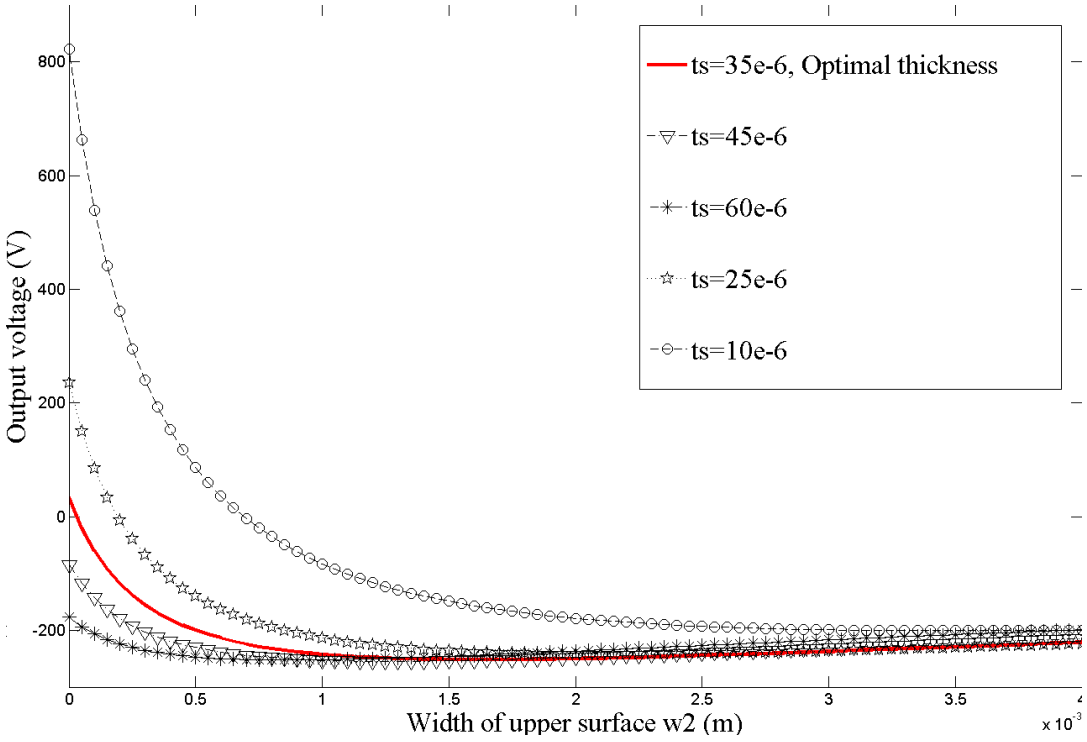

Figure 2.12 Effect by changing width of upper surface on average induced voltage, with five groups of thicknesses of SS layer

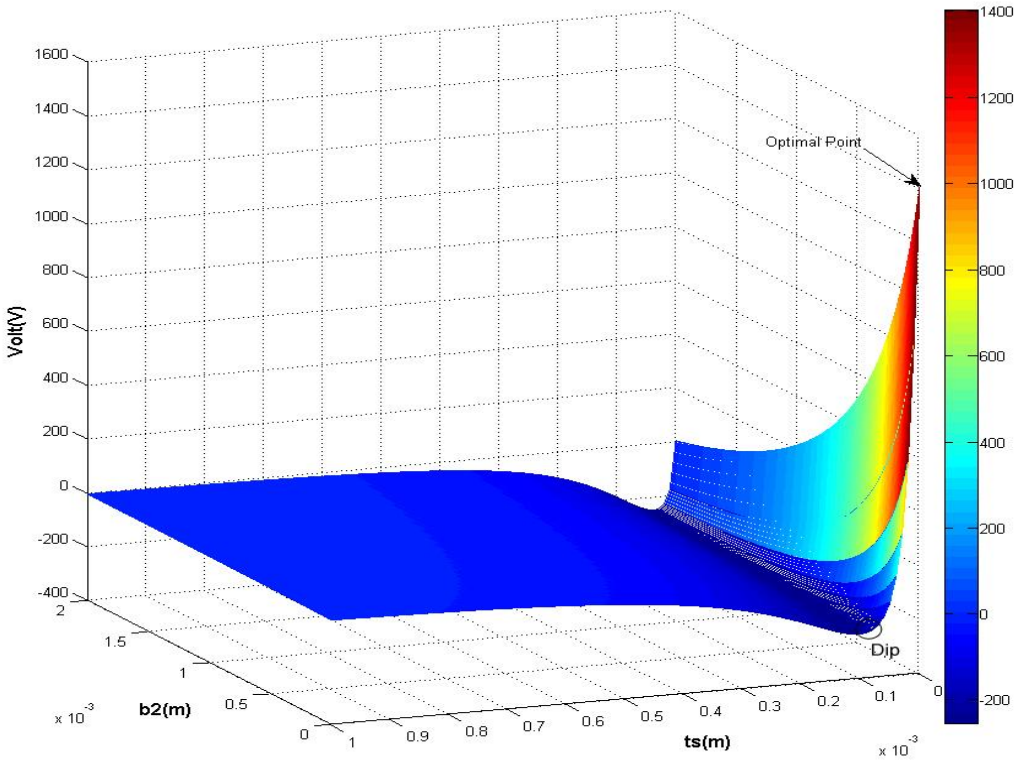

Figure 2.13 Average induced voltage distributions on upper surface width w_2 and thickness of SS layer t_s for first structure with trapezoidal cross section, maximum point occurs at (0, 0), which matches our previous prediction

For the first configuration, changing w_2 and t_s values, and keeping t_p and w_1 values constant results in the optimal point, which occurs at (0,0). As plotted in **Figure 2.13**, the optimal point is derived from a triangular cross section without a stainless steel layer. However, a dip is observed at (0, 0.05E-3) indicating that decreasing the thickness of the stainless steel layer causes the induced voltage to diminish tremendously. This is because for a cantilever with triangular shaped cross section under a static force input, the strain/stress on the tip is greatly intensified, as shown in **Figure 2.14** below. So by

replacing the part of the most strain/stress with non-piezoelectric material will significantly decrease the induced voltage that can be achieved. With a thicker SS, the neutral plain moves into SS layer, with only either compressive or tensile stress in PZT layer. This explains why induced voltage will increase again after the dip point.

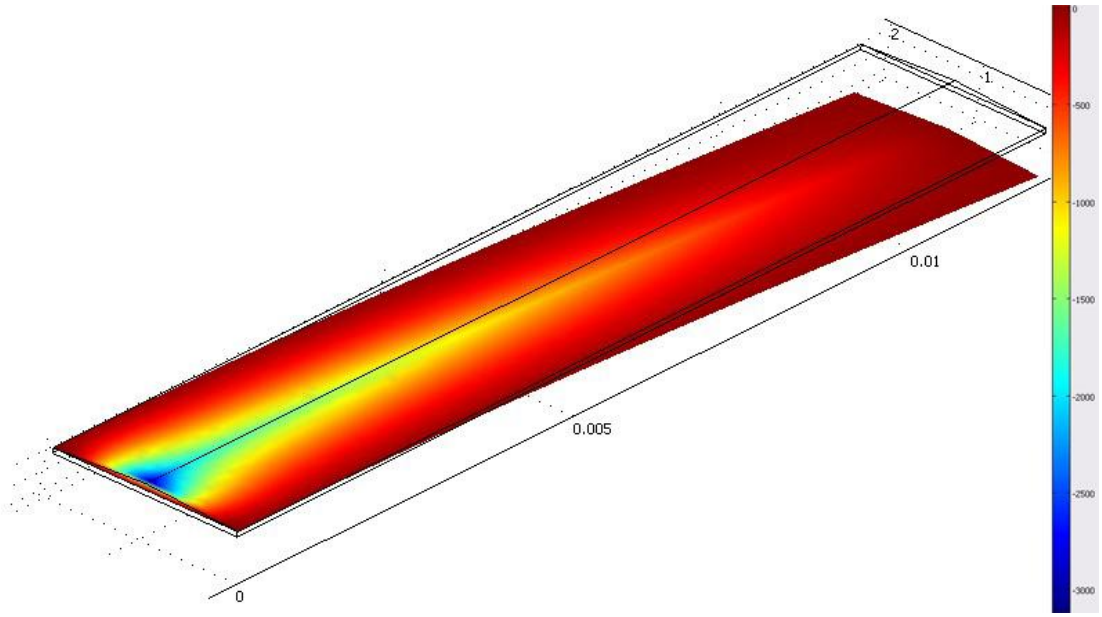

Figure 2.14 Illustration on strain distribution on piezoelectric unimorph with a triangular shaped cross section.

For second configuration, the thickness and the width of the SS layer are held constant, and it is assumed that $t_s = 50\mu m$ and $w_1 = 2mm$. The results for this model are plotted in **Figure 2.14.**

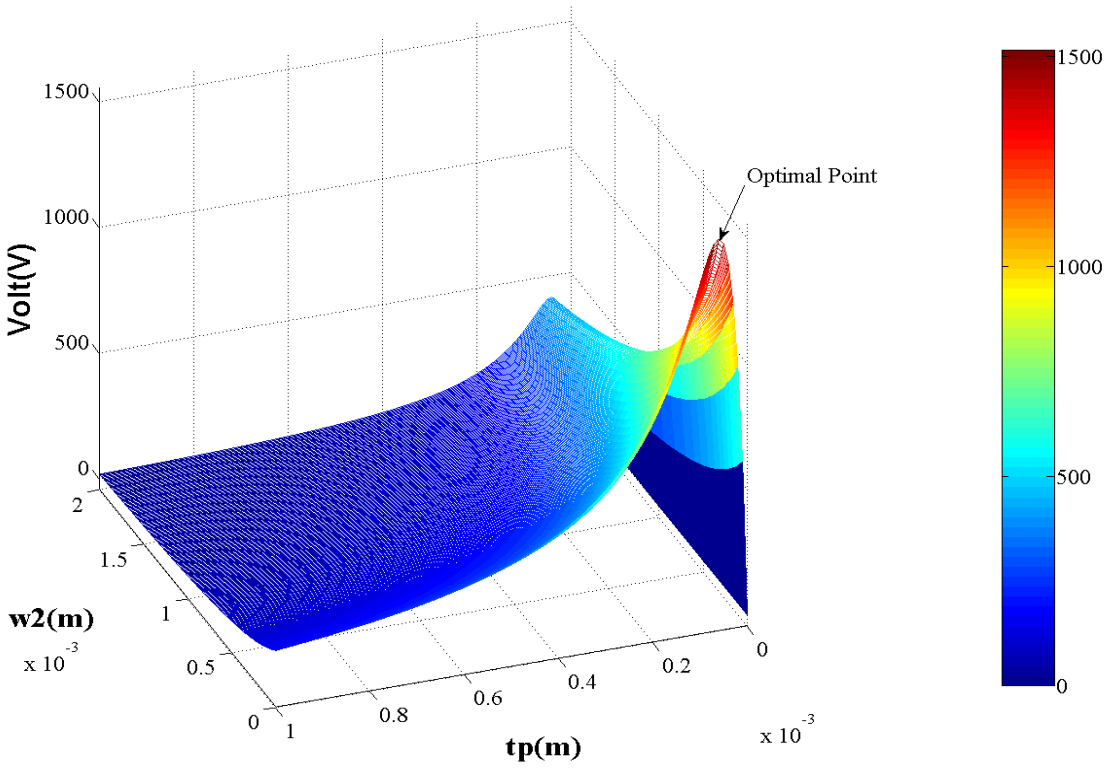

Figure 2.15 Average induced voltage distribution on upper surface width w_2 and thickness of PZT layer t_p for second structure with trapezoidal cross section, maximum point occurs at (0, 0.5841e-4)

We compared the optimized two configurations of Model 2 in finite element software, and FEM results match well with our theoretical calculations as seen in **Table 2-4**.

Table 2-4 Comparison of average induced voltage for two configurations of Model 2 at optimized geometries.

	Optimized Geometries (mm)				Average Induced Voltage (V)		
	w1	w2	ts	tp	FEM	Theo.	Error

Configuration 1	2	0	0	0.127	122	140	12.8%
Configuration 2	2	0	50	58.4	157	151	4.1%

From **Table 2-4**, we see that voltage in the kV level is possible for devices with small geometries. Based on the research of Staines, Hofmann *et al.* [68] the charging voltages in the range 100-1000 kV are possible based on the charging scheme and the number of piezoelectric devices used.

We have used the theoretical and FEM analysis to examine several geometries that are non-optimized in order to support our model. Comparisons are given in **Table 2-5**.

Table 2-5 Comparison of average induced voltage for two configurations of Model 2 at several non-optimized geometries

	Geometries (mm)				Average Induced Voltage (V)		
	1	2	ts	tp	FEM	Theo.	Error
Configuration 1	.5	0.04	0	0.127	-177.083	-200.62	11.7%
			0.05	0	0.127	-225	-234.011	3.9%
	.5		0.06	0	0.127	-225.875	-226.21	1.5%
Configuration 2	.5		50	40	889.5	801.07	11.0%
			50	50	611.25	585.84	4.3%

	5	6				2.6
.5	0	0	450.78	439.24		%

What should be noted is that all these results on induced voltage, thickness ratio, and optimal cross section can also be applied to dynamic models, like a piezoelectric vibration-to-electricity converter, since force F in **(7)** can be both static and dynamic.

2.4. Results and Discussion

The purpose of this study was to investigate performance of energy harvesters under static forces. Two theoretical models were developed for piezoelectric unimorphs of various geometries via Bernoulli–Euler beam theory and linear piezoelectric theory. One model is for cantilevers with variable surface shapes with rectangular cross sections, another for rectangular surface shapes with variable cross sections. Equations for average induced voltage were obtained for both cases, in terms of geometries, material properties and input forces. The expressions were employed in parametric studies for Model 2, to examine how geometries of different cross sections influence the average induced voltage. Our results showed that a trapezoidal shaped cross section enhanced the output voltage. Because the unimorphs are too thin and brittle to fabricate with trapezoidal cross sections, we could not conduct experiments to verify this portion of the work, and thus no experimental results were provided for the model where the cross section varied as is **Figure 2.3** and **2.4**. This study also revealed that the average induced voltage for Model 1 can be exactly the same under certain conditions (same surface area and length), no

matter how the surface shapes change. Finite element models were first studied in COMSOL to verify the theoretical model. The results were in good agreement with the theoretical predictions, thus proving the validity of our model and statements.

Chapter 3.

Experiments on Unimorph Piezoelectric Cantilevers with Non-traditional Surface Geometries

3.1. Sample Preparation, Setup and Configurations

A piezoelectric layer of 127μm thickness (T105-H4E-602, PIEZO SYSTEMS INC., Cambridge, MA, USA) was carefully cut by blades into wanted geometries, i.e. trapezoidal, triangular, rectangular shapes etc. A 50μm stainless steel layer (Type 304, Alfa Aesar, Ward Hill, MA, USA) was cut into the shapes that pair to the PZT layer. Conductive epoxy (CW2400, Chemtronics, Georgia, USA) was then applied to carefully to avoid shorting out the device. Nickel electrodes had been deposited on PZT layer so that by attaching leads on the upper and bottom surfaces, induced voltage along the thickness direction could be obtained.

In order to validate the prediction in Chapter 2 section 2 that if surface area, length are held constant, no matter how surface shapes change, the output voltage should be unique with the same static load experiments were performed. Experiments were setup as shown in **Figure 3.1. Figure 3.1** presents a illustration of the unimorph piezoelectric cantilever clamped by two glass substrates.

Figure 3.1 Illustration of the unimorph piezoelectric cantilever system, comprising of a cantilever, glass substrates, laser displacement sensor

A laser displacement sensor (LK G-10, Keyence Corporation, NJ, USA) was placed at the position of cantilever tip to detect the exact deflection when we applied a load at the tip. The displacement and induced voltage was captured using Agilent 34401A oscilloscope (Agilent, Palo Alto, CA, USA). A 10:1 oscilloscope probe is connected so that voltage could be measured.

When the probe is connected, the induced electric charges on surfaces redistribute in a short time and pass through oscilloscope, which leads to a drop of voltage. **Figure 3.2** shows the voltage signal consists of both positive and negative peaks. The positive peak happens when a weight is added at the tip and the negative one when weight is lifted. But of course the direction of peak depends on the poling direction of PZT layer.

Applying a weight at tip may cause a slight vibration, generating a hackle shape signal as shown in diagram. We take the spike value as the average induced voltage.

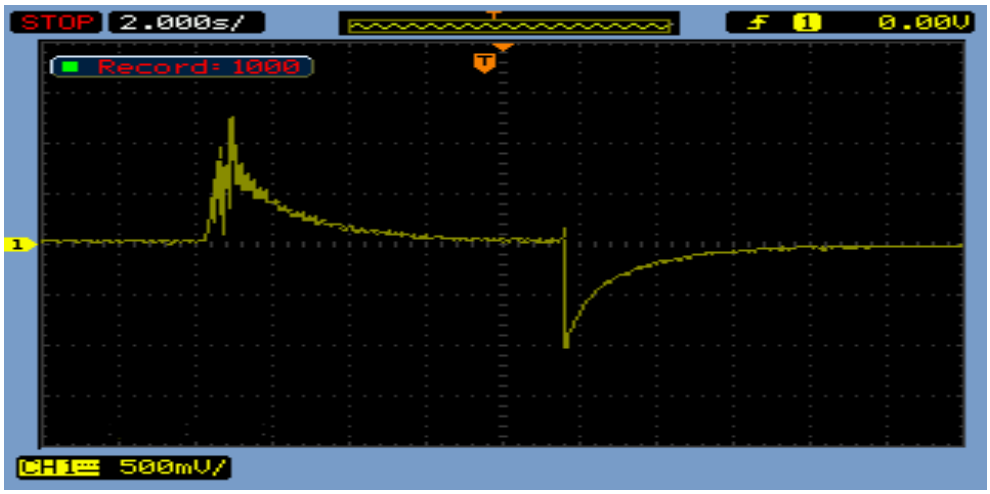

Figure 3.2 Voltage signal when a weight is applied/removed

These results can be explained by Roundy's work. Roundy [6] built an analytical model for piezoelectric transducers by modeling both mechanical and electrical portions of the piezoelectric system as circuit elements, which is shown in **Figure 3.3.** He gives the system equation as

$$\dot{V} = \frac{-Ydt_c}{\varepsilon}\dot{\delta} - \frac{1}{RC_p}V \tag{26}$$

It clearly shows that with a step load, if $\dot{\delta}$ is a positive value, $\dot{V}$ is positive too, which gives a positive spike as shown in **Figure 3.2**. When removing a load, strain drops to zero and the negative $\dot{\delta}$ gives a spike in the opposite direction.

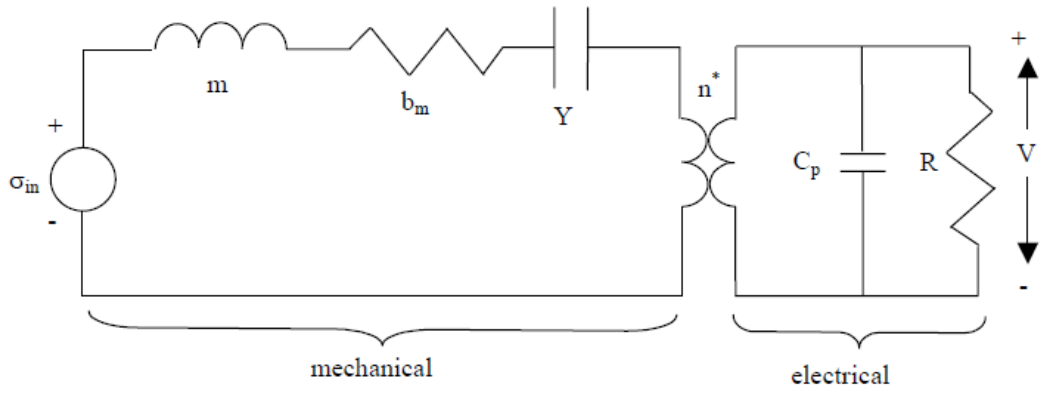

Figure 3.3 Circuit model of piezoelectric bimorph with resistive load

The samples that were fabricated are presented in **Figure 3.4**. The dimensions are shown in **Table 3-1**.

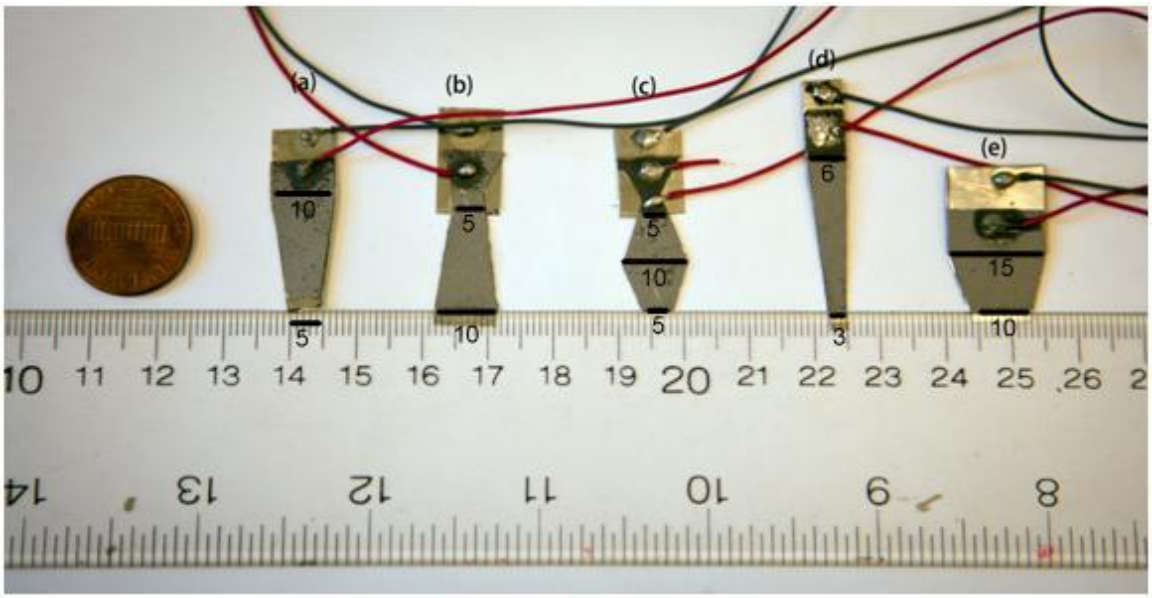

Figure 3.4 (a) trapezoidal shape; (b) reverse trapezoidal shape; (c) hexagon shape samples; (d) longer trapezoidal shape; (e) shorter trapezoidal shape. All samples from (a) to (e) have the same surface area.

Table 3-1 Dimensions of samples used in exp. validation

Model No.	Length (mm)	Left width b_1 (mm)	Right width b_2 (mm)	Surface Area A (mm^2)
(a)	15	10	5	112.5
(b)	15	5	10	112.5
(c)	7.5/7.5	5	5	112.5
Comparison Group				
(d)	25	6	3	112.5
(e)	9	15	10	112.5

3.2. Experimental results and discussions

The samples were subjected to weights that ranged from 350 mg to 850 mg, with intervals of 100 mg. In order to prevent variances from impulsive forces due to the addition of weights; weights were applied slowly and at a constant velocity. The devices were placed within close proximity and on anti-vibration table to reduce random vibration caused by air flow or walking.

Figure 3.5 shows the average induced voltage versus tip load for cantilevers with the same surface area but different geometries, and **Figure 3.6** compares experimental values with theoretical values obtained from equations (**12**) and (**14**). As we can see in **Figure 3.5** and **3.6**, cantilevers with the same area and same length have very close induced voltages, regardless of the shape of the surface. The fact is, when the same load is applied at the tip, the strain distribution should be as shown in **Figure 3.7**. We can see it is true that trapezoidal shaped cantilever has a lower slope at the root part (more evenly distributed), but it clearly indicates that before a certain position, 4mm in the *x* direction

in our example, all of the three other cases have a larger strain than the trapezoidal cantilever. Besides, also note cantilevers with same surface area but various lengths give significant increase/decrease on output voltage. That is reasonable because longer cantilevers have larger tip displacement than shorter devices when the same force is applied, and as expected, larger bending leads to higher induced voltages. **Figure 3.8** and **Figure 3.9** depict the reciprocals of the effective spring constants of samples. These figures illustrate the fact that longer devices have larger spring constants, and samples that have smaller root widths also have higher spring constants.

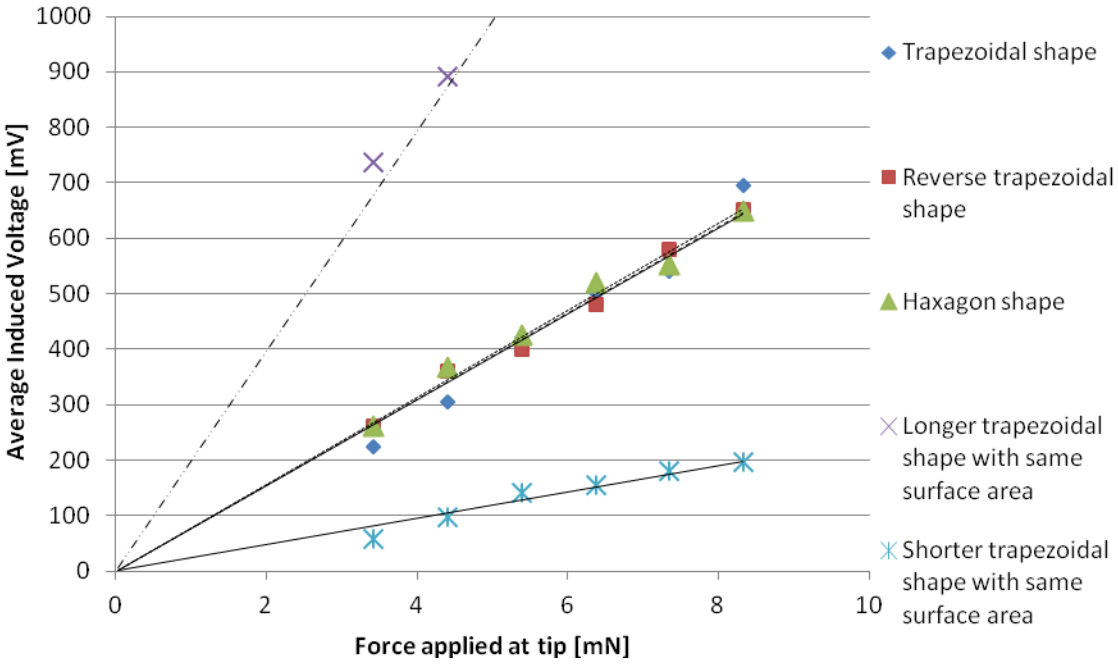

Figure 3.5 Average induced voltage per unit force applied at tip

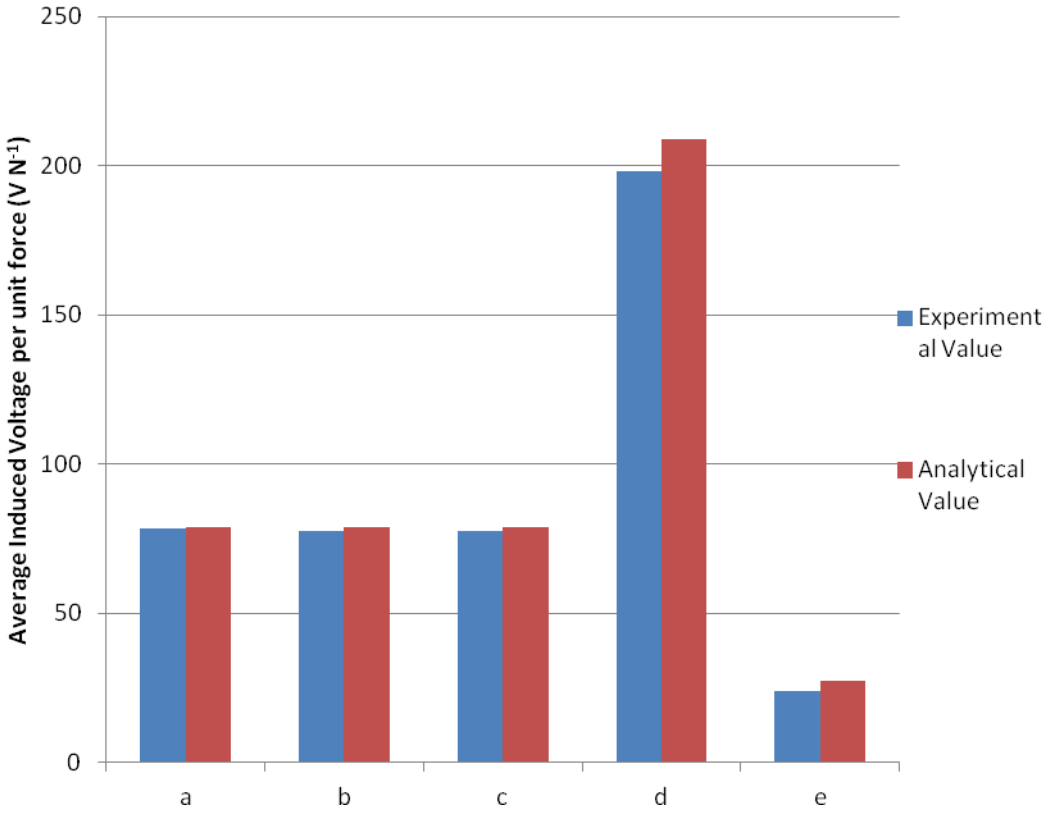

Figure 3.6 Comparison of experimental and theoretical results on average induced voltage per unit force for cantilevers with various geometries.

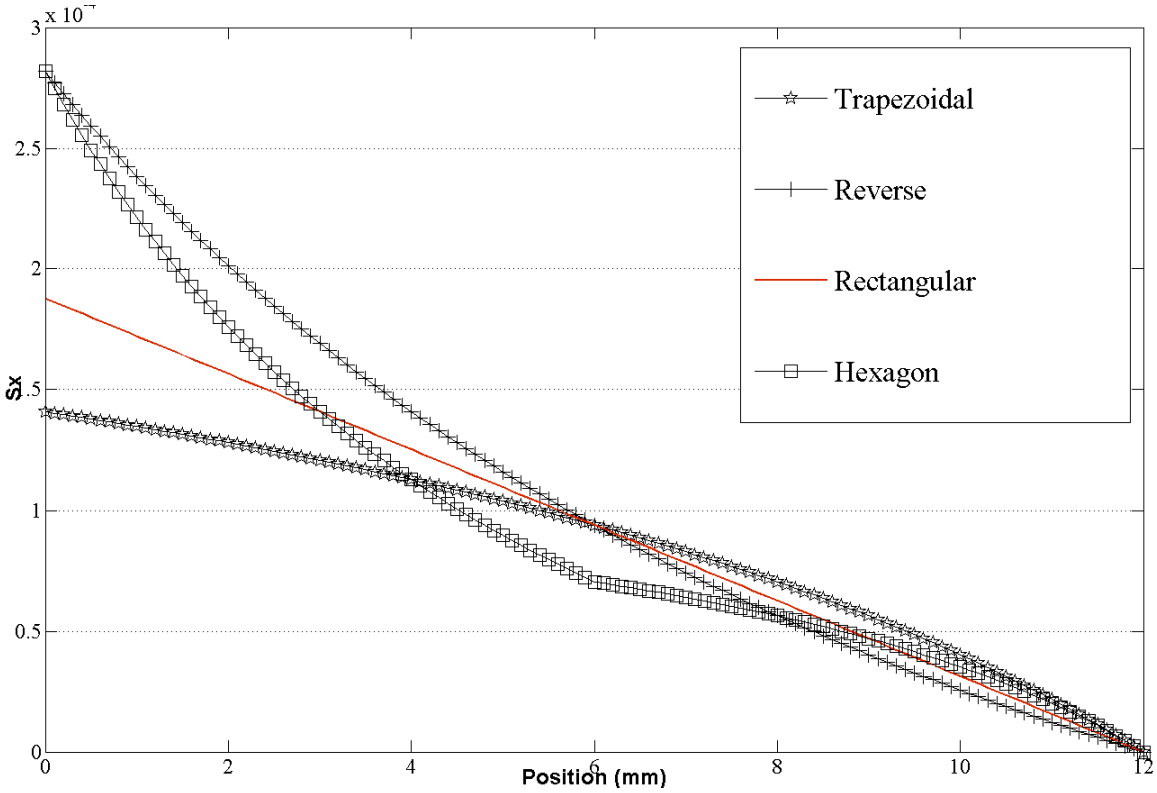

Figure 3.7 Strain distribution along length direction

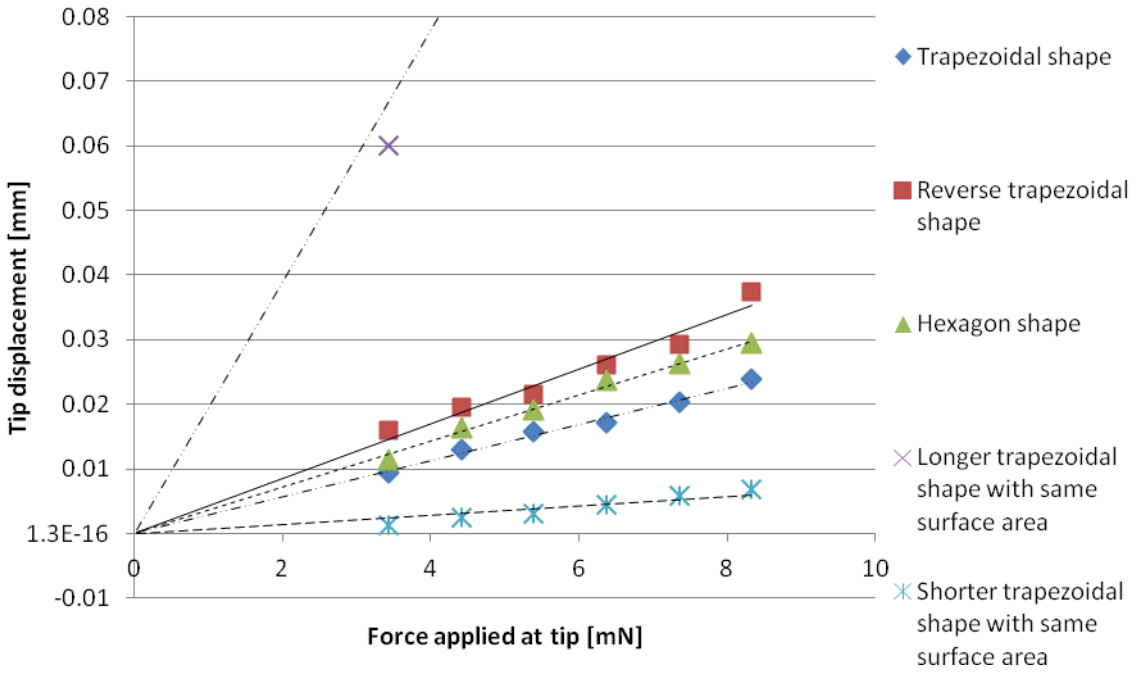

Figure 3.8 Reciprocal of effective spring constant

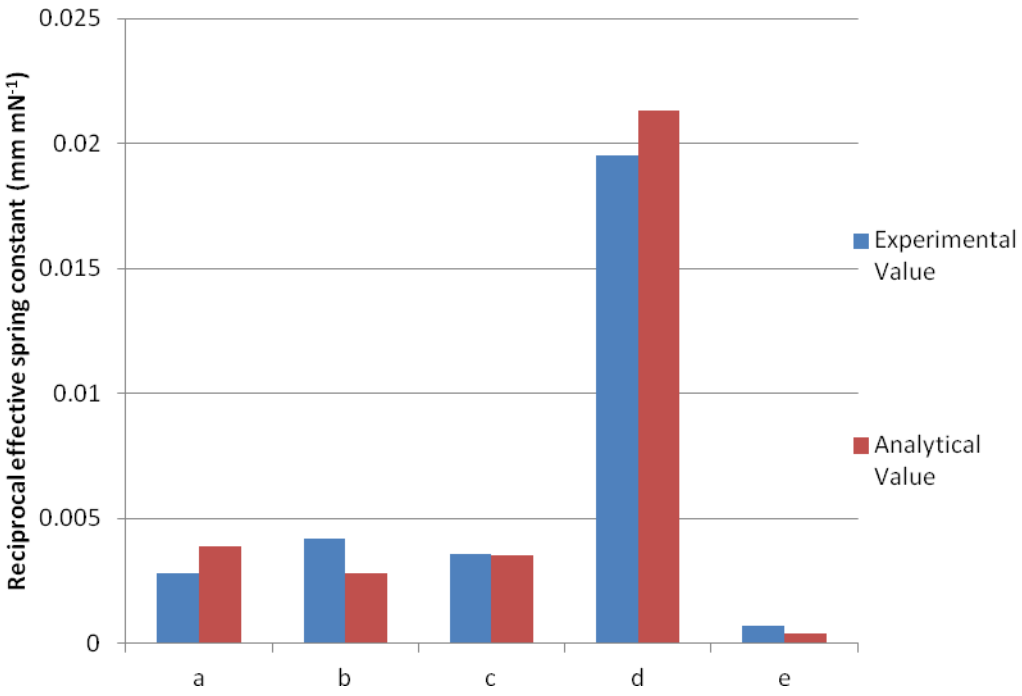

Figure 3.9 Comparison of experimental and theoretical results on reciprocal effective spring constant for cantilevers with various geometries

In **Figure 3.10** only (a), (b) and (c) samples are plotted, the data from the other samples are not shown within the plot area (to make the plot easier to interpret). In **Figure 3.11** shows the relationship between the induced voltage and displacement for samples. Unlike the previous two diagrams, **Figure 3.11** gives a relatively larger error in sample (e). For a short cantilever, bonding layer can play a role in strengthening the beam to some extent, which decreases the deflection. The same effect is actually also reflected in **Figure 3.6** and **Figure 3.9**, but not that obvious due to small absolute values of deflection. The trend is still in accord with theoretical analysis despite of the errors.

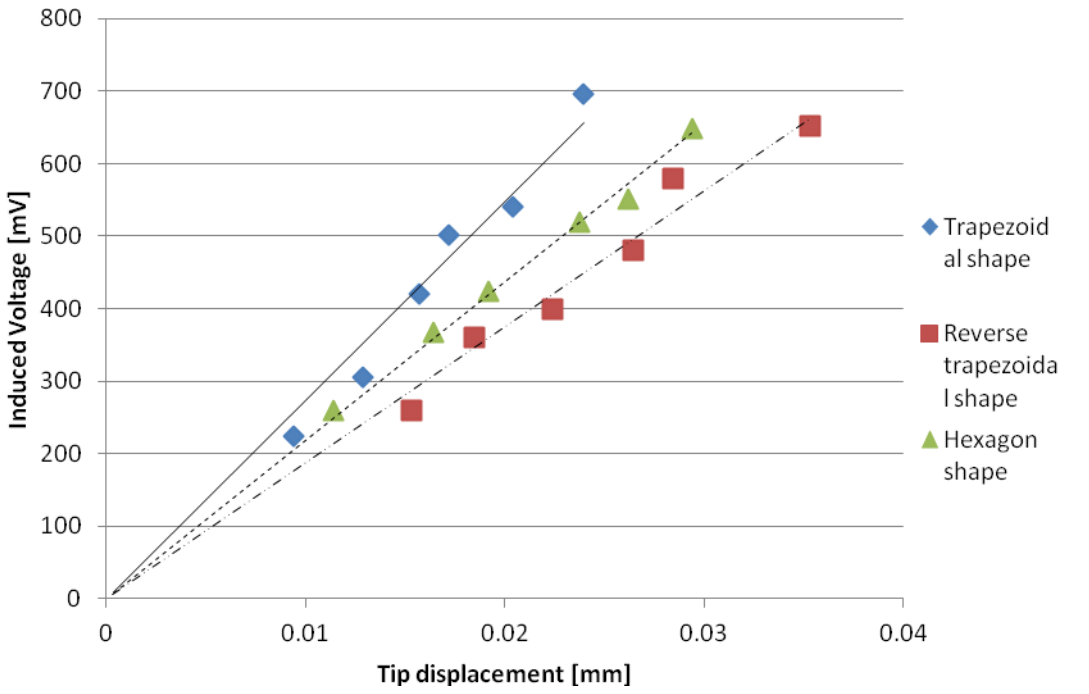

Figure 3.10 Average induced voltage per tip displacement

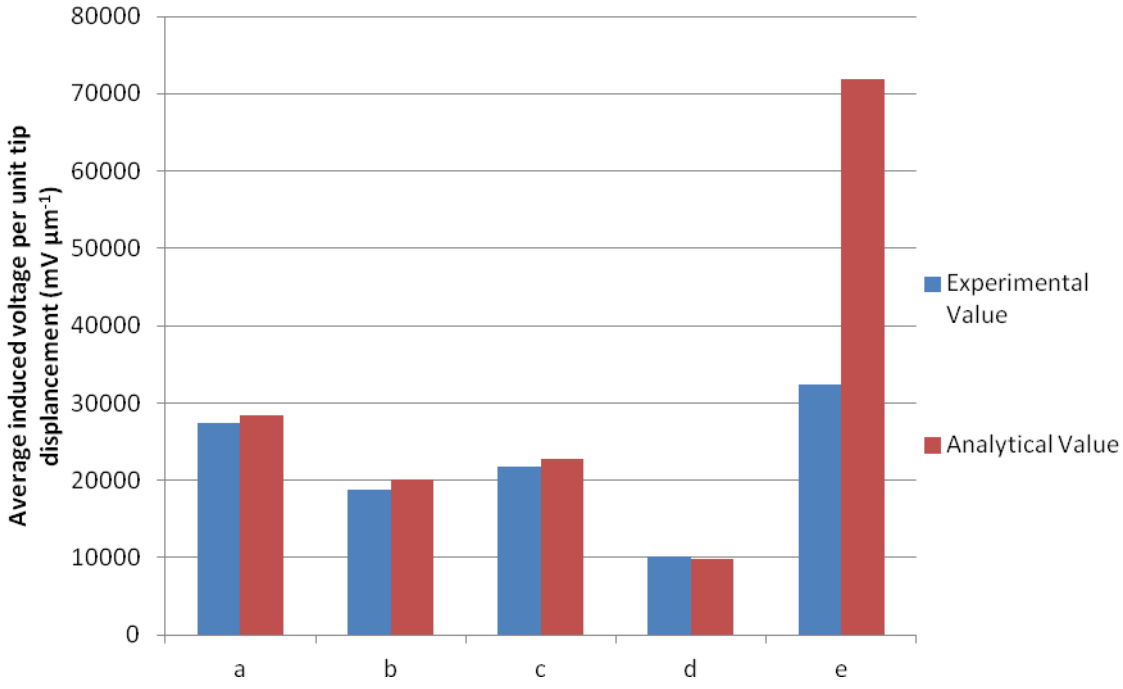

Figure 3.11 Comparison of experimental and theoretical results on average induced voltage per tip displacement for cantilevers with various geometries

Though induced voltage is a critical parameter to justify energy scavengers, stress limits should also be taken into consideration. As we can see from **Figure 3.7** and **Figure 3.8**, a cantilever with a narrow width on fixed end and a longer total length gives an intensive strain at the root, which can lead to cracks during operation. Thus fracture criteria must be considered for product design.

Based on this work we can make several conclusions regarding piezoelectric energy harvesting devices:

- For a given thickness of piezoelectric layer, the average induced voltage on the unimorph cantilever device depends on the total length of the device, applied load at the tip and surface area of the device. If the applied tip load and device length are held constant, while the shapes are changed, all cantilevers will produce the same average induced voltage;
- Designing a longer PZT unimorph cantilever gives higher average induced voltage, compared with shorter ones with same area. In other words, to achieve certain amounts of voltage, a narrow harvester can reduce both the size and cost;
- If the device is too narrow at the fixed end, breakage of the device can result, so fracture criteria of applied piezoelectric material should be studied;
- If designing a thick device, an optimal trapezoidal shaped cross section can be made to enhance its average induced voltage at the same load.

Chapter 4.

Fabrication of Dome-shaped Piezoelectric Energy Harvesters

4.1. Introduction

As we mentioned in Chapter 1, the brittle nature of homogeneous PZT material limits their application in harsh environments where they would experience high strains/stresses. The brittle nature of these materials also limits the shapes that they can be fabricated into. Others workers have examined piezocomposites [14, 16, 26, 27, 40, 41, 43, 44, 46, 47, 69-73]. Among the various connectivity patterns 0-3 connectivity lends itself to synclastic curves and shapes, and this shape is amenable and useful for application to hydrophones and energy harvesting devices envisioned for static loading and tapping. The fabrication procedure for 0-3 connectivity is less complex than the fabrication techniques for many of the other connectivities. This type of fabrication technique requires low mass production cost and offers the potential to fabricate various structures using coating techniques. By illustrating the dome-switch keyboard mechanism in Chapter 1, we explained the feasibility to assemble the dome-shape piezoelectric energy harvesters into input devices. In this chapter, our work will focus on fabricating dome-shape piezoelectric energy harvesters by spin coating and sol-gel techniques. Specifically, the surface images, strain coefficient, capacitance will be observed.

Mohamadi *et al.* [69] dispersed PZT fibers of different diameters into an epoxy matrix, which makes the up ~40% PZT volume fraction and remaining 60% of epoxy. Their devices possessed a piezoelectric coefficient of 300 pC/N, and could generate 120mW of peak power when a 33g stainless steel ball was dropped on the transducer. Banerjee *et al.* [48] examined the influence of Al particle size and PZT volume fraction on the dielectric properties. These samples were also were comprised of various volume fractions of PZT and Aluminum particles into epoxy matrix.

Although dome shaped piezoelectric structures are not new, the fabrication technique posed here for the fabrication of the dome shape is to our knowledge, novel. Though research on dome-shaped piezoelectric transducers/sensors/actuators has not been extensively done, some recent studies on fabrication techniques, different functional materials, structure and geometries etc. show that there is great potential of the dome-shaped configurations. Guo-Hua Feng and his coworkers [22-24, 55] have published several papers on their MEMS dome-shaped-diaphragm transducers and applications. They use spherical balls on thru holes of a silicon wafer to make the dome shape mold in molten wax, and then deposit an electrode, piezoelectric layer, and insulting layer in sequence to fabricate transducers [24, 55]. They have also analyzed the energy conversion efficiency of these dome-shaped transducers for application as micro generators using an equivalent circuit. Besides, power output of different piezoelectric materials, piezoelectric/insulating/mass loading layers thickness, and dome curvature radius were also examined by going through the equivalent circuit mathematically [22]. They also assembled their dome-shaped-diaphragm transducer with two one-way valves

to form a micropump, which had a total geometry of $10\times10\times1.2$ mm^3. This device consumed very low power (i.e. 3mW to pump 3.2μL/min) and possessed negligible leaks [23]. Yoon Man-Soon *et al.* [8] fabricated dome-shaped piezoelectric actuators by powder injection molding using a $0.04Pb(Sb_{0.5}Nb_{0.5})O_3$-$0.46PbTiO_3$-$0.5PbZrO_3$ composition. The two actuators they made were 5mm and 8mm diameter in shape, with the same curvature radius of 10mm. The actuators were poled at 150 ^oC at 2.5kV/mm for 40 min. The dome-shaped piezoelectric actuator samples tested revealed that the maximum tip displacements in the 8mm and 5mm samples were 700 and 300 nm, respectively. Safari *et al.* [74] from Rutgers University used PMN-PT 65/35 powder as piezoelectric material and PMN-PT 90/10 powder as electrorestrictive material to fabricate a bilayer P/E dome unimorph. Powders were mixed separately with polyvinyl alcohol solution and then heated and sieved to get fine powders. Powders of piezoelectric and electrorestrictive materials were compressed uniaxially to form a 1.2 mm thick bilayer sample. The composite interface was called a *functionally gradient material*. His work demonstrated that a functionally gradient material yields better field-induced strain, while reducing mechanical stress in comparison to standard bimorphs and unimorphs. The samples were poled at 150 ^oC for 10 min under 2.5kV/mm voltage. Dome heights varied from 0.3 mm to 0.46 mm. The piezoelectric coefficient, d_{33} (370-550 pC/N), electromechanical coupling, K (3370-4370) and tanδ (1.72-2.26) were measured [74]. Safari also analyzed the dome-shape unimorph actuator model in FEM software for three types of poling directions: 1) thickness poling direction; 2) tangentially poling direction and 3) tangentially alternating poling direction. The dome geometric parameters, polling direction, electric field and material properties were taken into account. No mathematical

derivation was mentioned in this paper, but still the idea for three polling directions are novel. The FEM results showed that compared to other two poling directions, one alternating tangentially poled dome actuator has larger displacement and force responses.[75] Some researchers have studied and the RAINBOW method to develop dome shape devices. This method uses the different thermal expansion coefficients between the piezoelectric layer and non-piezoelectric layer to produce the dome-shaped. For example, Shen [73] studied the manufacture, structure and properties of RAINBOW piezoelectric transducers. He pointed out that the reduced layer was transgranularly fractured while the unreduced ceramic was intergranularly fractured. Two kinds of fracture types were seen at the interface, which denotes the different degrees of reduction. Cheng *et al.* [11] compressed PZT-5H powder into a compact solid, and glued it onto a thin stainless steel substrate, and cured at 120 ^{o}C for 2 hours. The difference of the thermal expansion between PZT and steel produced the domelike structure. Workers have also electroplated the piezoelectric actuator module for a different time, in order to induce more arch shaped structures and enhance loading ability. Buchanan *et al.* [76] fabricated a RAINBOW type high displacement actuator from Nd and Zr doped Barium Titanate. The powder that contained BT and dopants was pressed twice to fabricate bilayer pellets or three times to make three layer pellets. They were able to show that the value of d33 of BT ceramics doped with Nd_2O_3 and ZrO_4 can exceed 500 pCN^{-1}. Three layered systems have higher electromechanical responses than two layered ones, indicating that compositional grading could cause different results in amplification of strain response. Goo *et al.* [14]expanded the concept of ‘layer’, and fabricated five-layer piezoelectric composite actuators using PZT ceramics, glass-epoxy prepreg, and carbon-epoxy prepreg.

The samples were asymmetrically laminated, which means the piezoelectric layer was not on the neutral plain, so that after applying the external voltage, expansion of the piezoelectric layer forces the assembly to bend. Three samples were fabricated. The flexural displacement under different loads was measured for a simply supported boundary condition and a fixed-free boundary condition. The stored elastic energy and neutral plane for each piezoceramic actuator was calculated and the deformation with different applied electric fields was measured. Peng *et al.* [28] proposed a dome-shaped piezoelectric transducer with very small initial deflection and analyzed it using FEM software. In this work the membrane electro-induced deflection over the base material thickness and initial dome height; effective coupling coefficient over substrate thickness and initial dome height was studied. They found that compared to conventional flat piezoelectric transducers, the dome-shaped device had an improved electro-induced deflection.

By illustrating the dome-switch keyboard mechanism in Chapter 1, we explained the feasibility to assemble the dome-shape piezoelectric energy harvesters into portable electronic devices with touch pads. In this chapter, our work will focus on fabricating dome-shape piezoelectric energy harvesters by spin coating and sol-gel techniques. Specifically, the surface images, strain coefficient, capacitance will be discussed.

4.2. Fabrication procedures

40% volume fraction PZT powder manufactured by READE International and Epoxy Resin (DGEBA, Epofix^{TM} Cold-setting embedding Resin) manufactured by

Electron Microscopy Sciences were mixed together with 2.5ml ethanol. Ethanol works as a binder to mix the PZT powders with epoxy. It is then evaporated out during the following procedures so that the composites only contain PZT and epoxy. The mixture was stirred in a sonicator using a stainless steel rod for 15 minutes to prevent formation of PZT clusters. An epoxy hardener was then added, and the new mixture was placed on a hotplate at 75 ^{o}C. The mixture was stirred until it became gel-like. The paste was then dispensed on the center of a pre-pressed dome shape stainless steel mold (Type 304, Alfa Aesar, Ward Hill, MA, USA). The mold was then placed into spin coater (WS-400, Laurell Technologies Corp.). The rotation speed of the spin coater was varied from 800 rpm to 2000 rpm depending on viscosity of the paste. A thin film formed by the balance between centrifugal force towards the edge and the drying rate, which affects the viscosity of the resin. After formation of thin film, the sample was post-cured at 75 ^{o}C for another 6 hours, allowing the film to turn into a solid layer. By repeating the spin process, thickness can be varied. The sample was then placed in a mold and poled under high voltage with the device illustrated in **Figure 4.1**. The high voltage supply was varied from1 to 130 kV (provided by SL Rack mount Power supply from Spellman Inc). Thickness of samples' poling voltage, poling time and temperature are summarized in **Table 4-1**, and geometries of dome-shape mold are illustrated in **Figure 4.2**. Poling under the Curie temperature creates (usually above 150 ^{o}C) the dipole movement of the central ion into the perovskite structure. Some of the samples fabricated are presented in **Figure 4.3**.

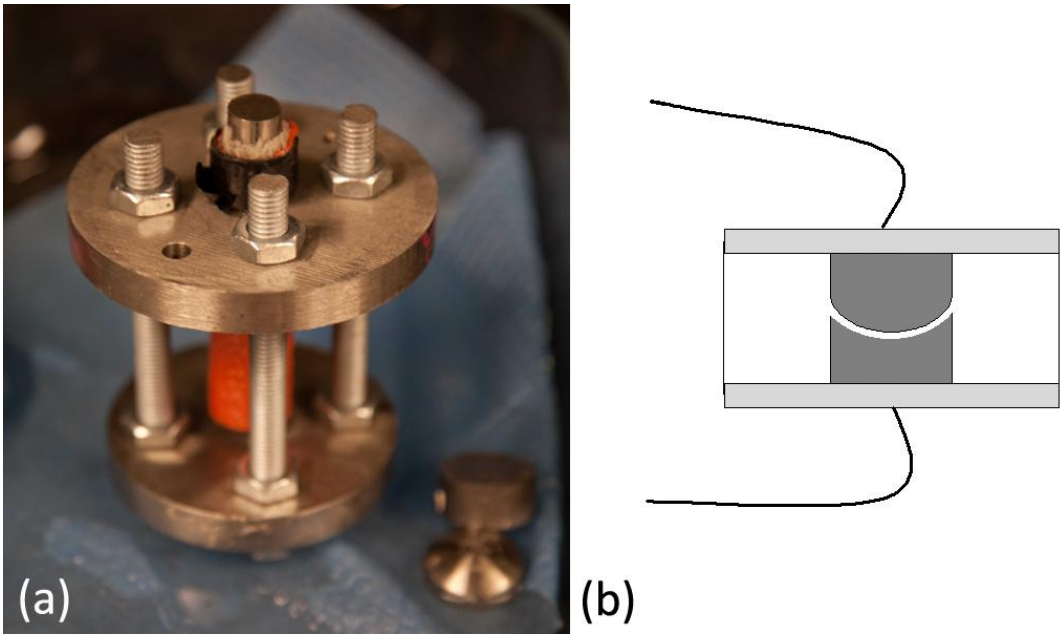

Figure 4.1 (a) Poling device fabricated by Mr. Sankha Banerjee; (b) illustration on connection.

Table 4-1 Polling conditions for dome-shape samples

Model No.	Thickness (mm)	Poling voltage (kV)	Poling temperature (^{o}C)	Poling voltage over thickness (kV/mm)	Poling Time (min)
(1)	0.292	0.5	80	1.7	30
(2)	0.366	1	80	2.7	30
(3)	0.292	1	80	3.4	30

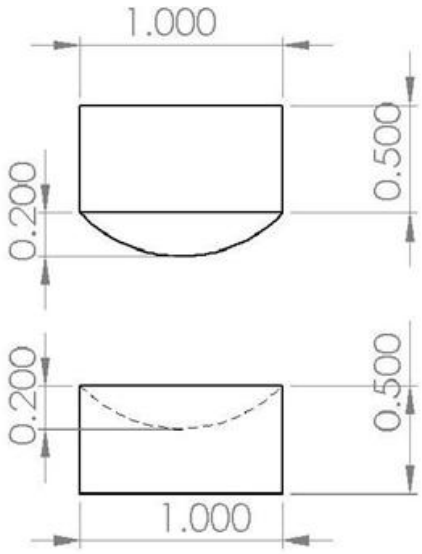

Figure 4.2 Geometries of mold used for dome-shape substrate and poling

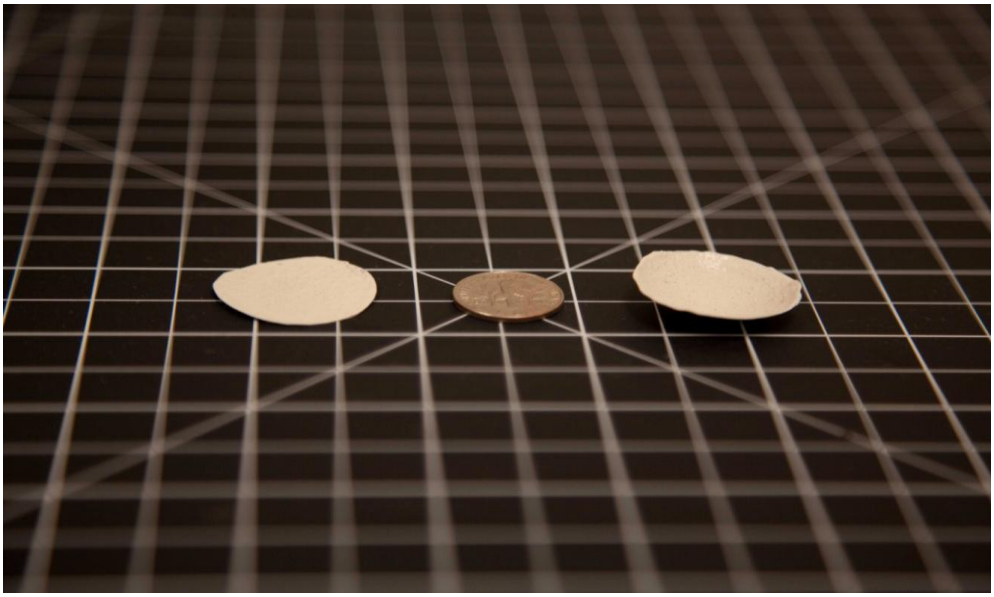

Figure 4.3 Plate and dome shape piezo-epoxy composite on stainless steel substrates

4.3. Results and Discussion

4.3.1. Surface examination

Two AFM images generated by one scanning under contact mode imaging: height image and deflection image are provided in Figures **4.4 (a)** and **(b)**. The height image contains the height information on a 30 by 30μm surface. Darker color indicates the deeper surface and lighter color gives the higher. The same is also true for deflection image. The contact mode means that the AFM tip is brought in contact with the sample surface with a constant deflection. The piezoelectric element driving probe scans every point on x-y coordinates while moving in the *z* direction, which is recorded to plot the height diagram. A laser diode beam shines on top of the cantilever and is then bounced towards a photodetector to record the cantilever deflection, giving the deflection diagram according to time interval.

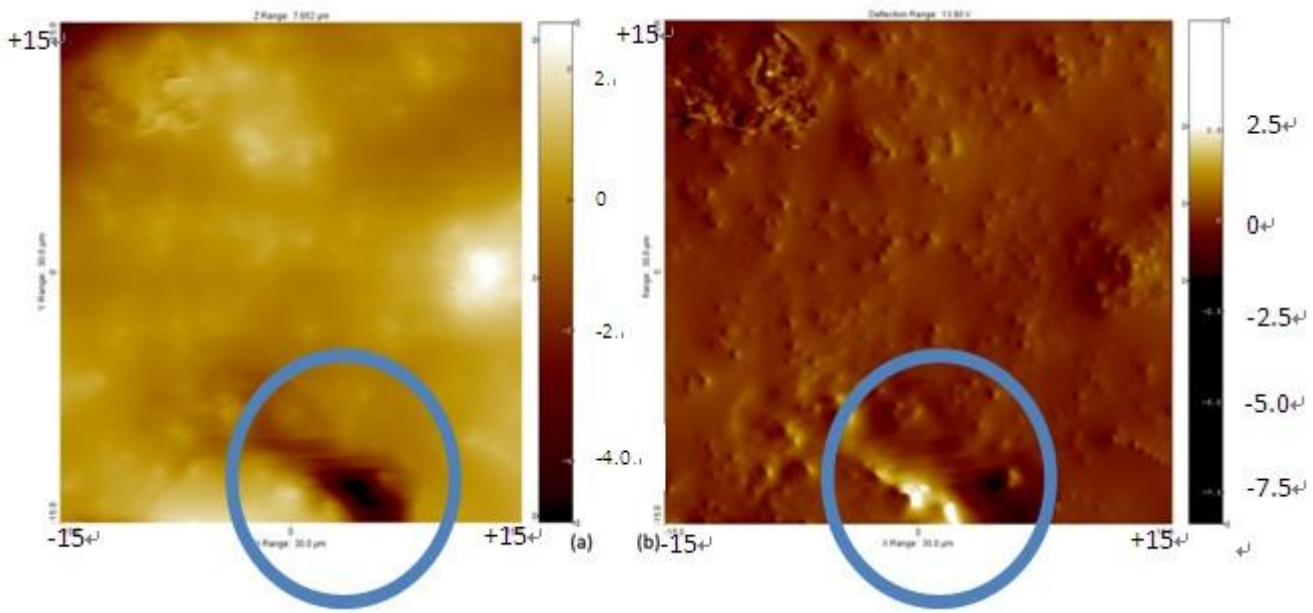

Figure 4.4 AFM micrographs of PZT-epoxy composite with PZT volume fraction of 40% at a 30 by 30 μm surface area. (a) height image and (b) deflection image. Unit: um.

The two scanning images on the same surface area do not look quite the same. The height image seems smoother, while the deflection image indicates many coarse surface particles which cannot be seen on height image. This is because the height image preserves the true height information of the sample, while in the deflection image; the tall features represent regions of higher degree of cantilever bending i.e. higher contact force, thus making the deflection image loose the true height information. Though the deflection image does not give the correct height data, it presents more fine details of the sample because the feedback loop response is faster for correcting the position of the small cantilever in comparison with correcting the position of the piezoelectric element. [77] From the height data, we have plotted a 3D image as shown in **Figure 4.5 (a)**. The

average profile on one cross section is given in **Figure 4.5 (b)**. The deflection data are also summarized in **Figure 4.6 (a)** and **(b)**.

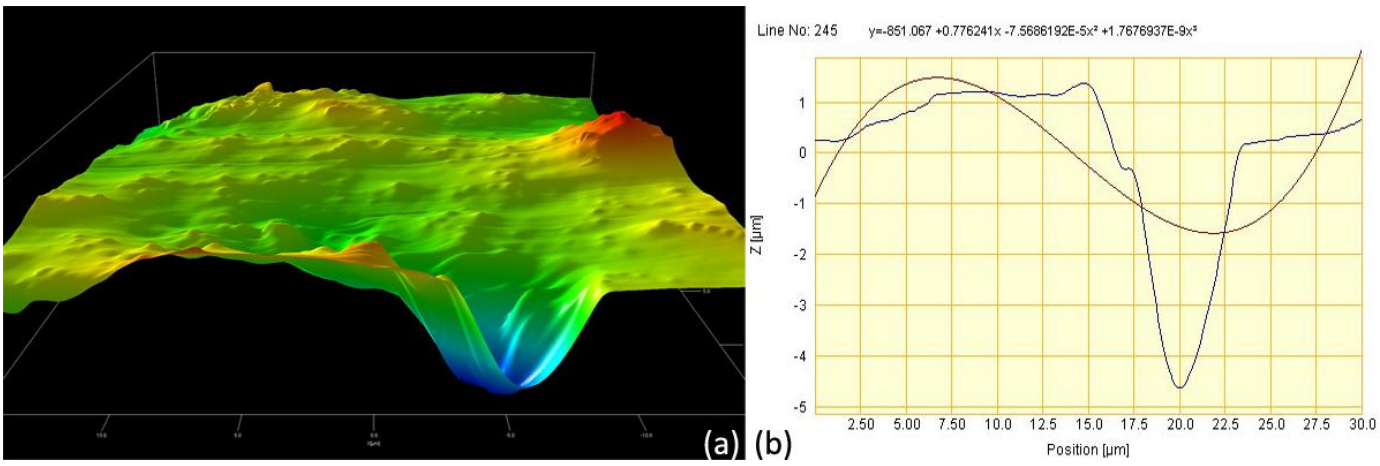

Figure 4.5 (a) Three dimensional simulation regarding height data; (b) Height of cross section at y=5µm.

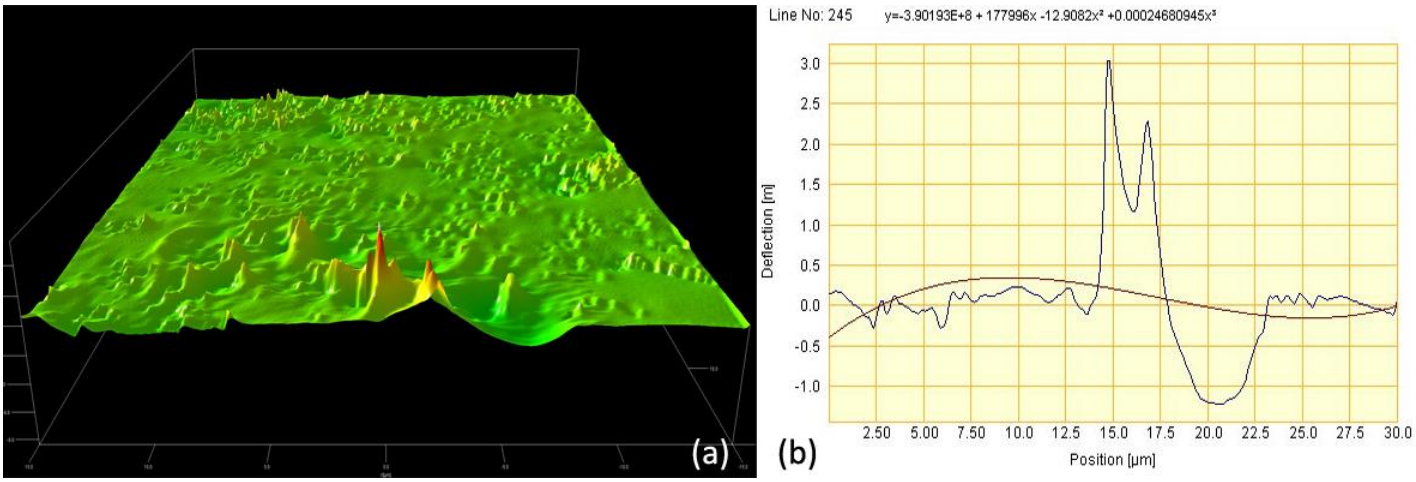

Figure 4.6 (a) Three dimensional simulation regarding deflection data; (b) Deflection of cross section at y=5µm.

Figure 4.5 illustrates a concave structure of -4.5µm deep, which may be induced by escape of an air bubble. Air bubbles come from the air-gel boundary during mixing

and sonication, and escape from the gel during heat treatment, leaving a cave like shown above in blue circle. **Figure 4.6** also indicates a fairly uneven surface, recording the roughness of the plain. The arithmetic average of roughness is calculated as Ra= 519.153 nm. Those coarse granules on surface represent PZT clustering, which was also clearly observed by one SEM image taken by Mr. Sankha Banerjee, shown in **Figure 4.7**.

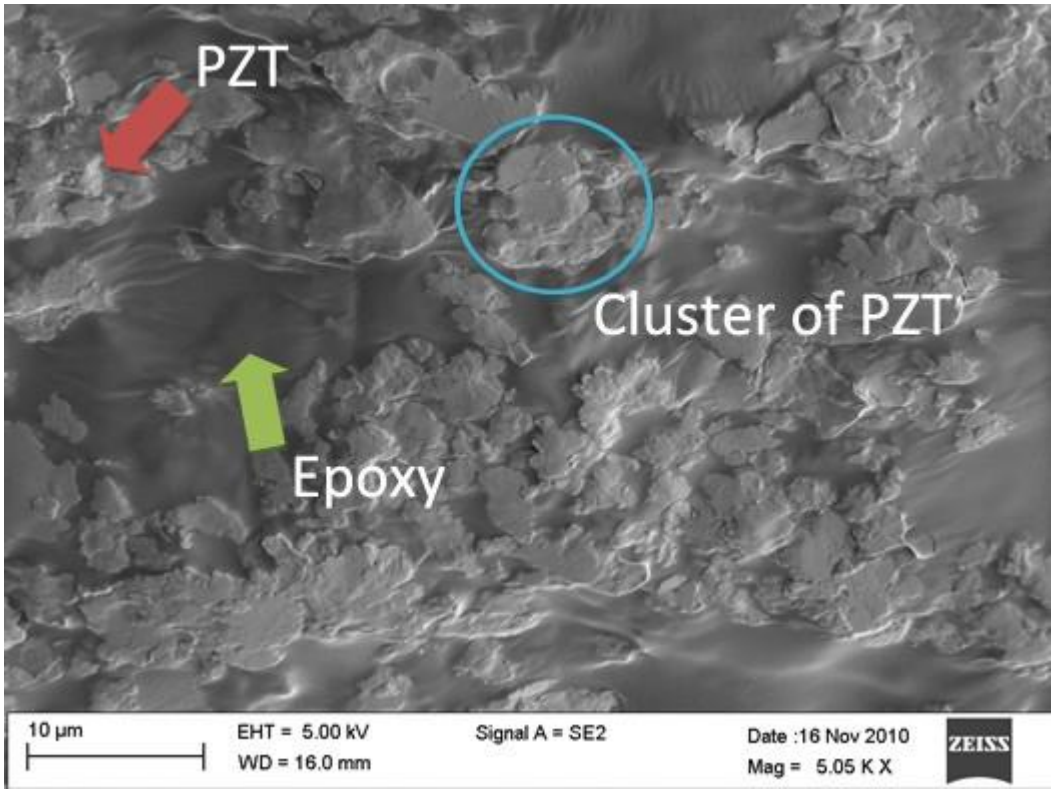

Figure 4.7 SEM micrographs of PZT-Epoxy composite with PZT volume fraction of 50% and magnifications of 5000 [Banerjee]

Those accumulations lead to the coarse peaks shown in the AFM images. The surface tension of the epoxy during sonication pushes the PZT particles together, which results in the formation of clusters of PZT. Reducing PZT particle size, increasing

sonication time, or using stronger sonication strength can cause a more evenly distributed surface area. However, the strong surface tension of epoxy makes it very difficult to eliminate this phenomenon.

4.3.2. Mechanical and Piezoelectric properties

We measured the piezoelectric coefficients d_{31}, d_{33} and capacitance, *C* using a PiezoMeter PM300 systems [PiezoTest Inc]. An illustration for d_{31} measurement configuration is shown in **Figure 4.8**. The basic mechanism of measurements for d_{31} and d_{33} is the straight application of direct/indirect piezoelectric effects. A high piezoelectric coefficient usually indicates a higher electric field developed per strain applied. A high frequency vibration is added on one direction (for example *z-3* direction), and a probe for detecting electric signals is connected on either *z-3* direction for d_{33} measurement or *x-1* direction for d_{31} measurement. The capacitance is simultaneously calculated at same time with d_{31}/d_{33} measurements. Capacitance has to be taken into consideration when developing the drive electronics, or matching an actuator to existing driving electronics. Results are all listed in **Table 4.2**.

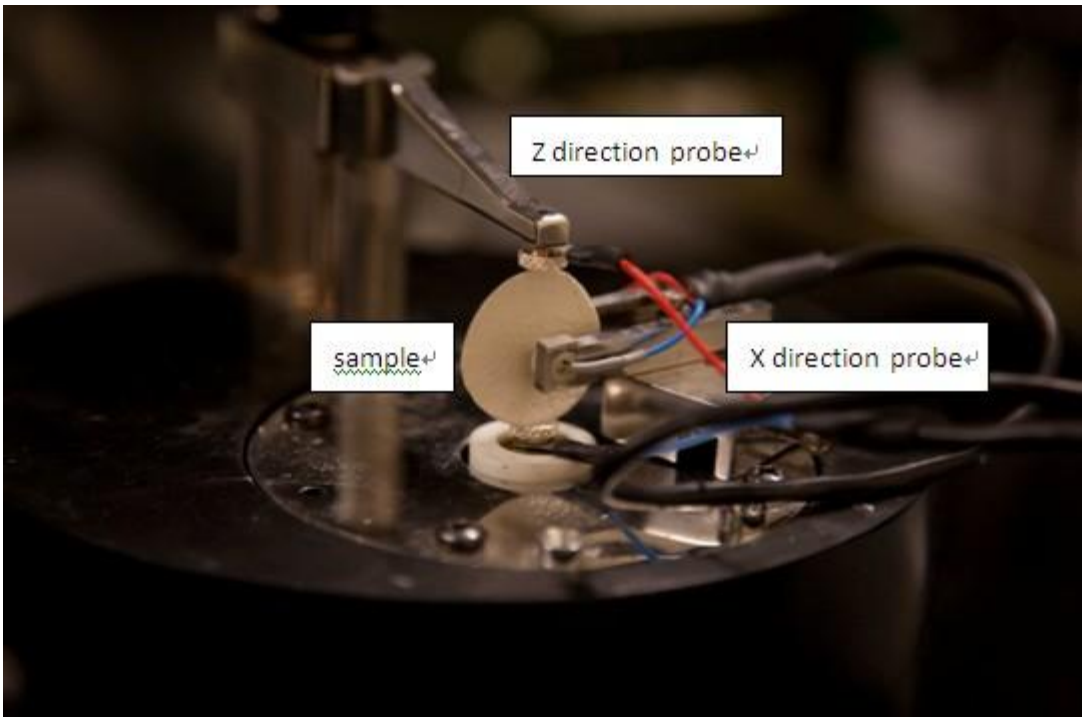

Figure 4.8 Illustration of d31 measurement on a plate shape sample by PizoMeter PM 300.

Table 4-2 Comparison of two dome-shape samples on d31, d33, and capacitance

Model No.	Thickness (mm)	Poling voltage (kV/mm)	d_{31} (pC/N)	d_{33} (pC/N)	Capacitance (pF)
Dome (1)	0.292	1.7	0.44	0.04	4.8
Dome (2)	0.366	2.7	0.51	0.85	6.3
Dome (3)	0.292	3.4	0.30	1.10	5.5

From Table 4.2 it clearly indicates a dramatic increase in d_{33} from 0.04 pC/N to 1.10 pC/N with increasing poling voltage, while d_{31} and capacitance do not change that much. The trends for these parameters are plotted in **Figure 4.9** below. Note that currently we do not have enough samples to understand the complete trends that result from increasing the poling voltage. However, we report the results we have recorded

thus far in this study. Experiments also indicate an upper limit of 4 kV/mm poling voltage for a 0.3 mm thick dome-shape sample, wherein higher poling voltages resulted in the sample breaking. The fabrication of more samples is required to fully understand the trends of the behavior of these type of devices.

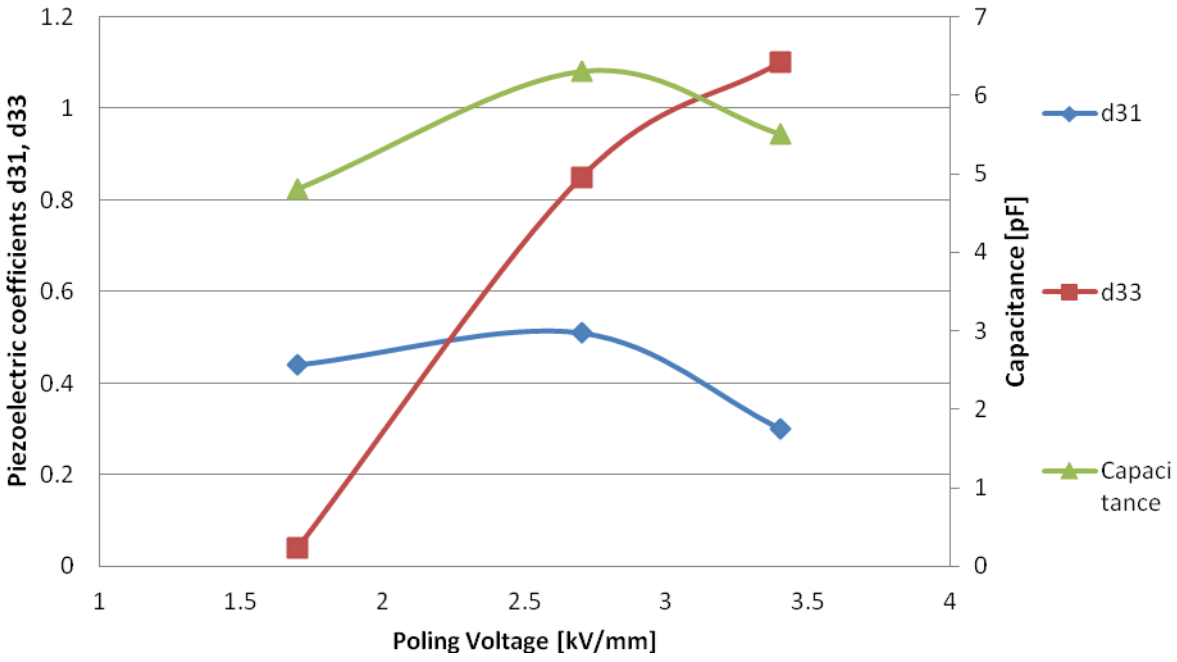

Figure 4.9 Trends of d31, d33 and capacitance with increasing poling voltage

Chapter 5.

Conclusions and Future Work

5.1. Conclusions

In this work we have performed a systematic study of piezoelectric unimorphs with non-traditional surface shapes that are comprised of one PZT layer and one stainless layer. Theoretical calculations, derived from piezoelectric constitutive equations for isothermal cases have been performed; and have been used to inform the relationship between average output voltage and surface shapes of the devices when subjected to mechanical loading. Our work shows that with the same input force applied to the tip of a device of same length and same surface area (no matter what kind of surface shapes are) the output voltage will be unique. This finding is critical in pushing the science of piezoelectric energy harvesting forward. In order to verify our theoretical calculations, we developed FEM models with non-traditional geometries but same length and surface areas. We compared average output voltage per unit force/displacement, and the spring constants with our model predictions, and they match very well. Five groups of piezoelectric unimorphs were fabricated for further validation, and showed a very good agreement with both the theoretical analysis and FEM calculations. Though our conclusion indicates surface shapes are not a keen parameter in respect to output voltage, a narrow width on the fixed end and a longer total length gives an intensive strain on the root of the device, which leads to cracks during operation. Thus surface geometries still should be considered for product design.

We also conducted optimizations of the unimorph cross section using Matlab. This allowed us to understand how geometries of variable cross section influence the induced voltage of the device. Our findings showed that a trapezoidal-shaped cross section could render an optimal output voltage, however due to the usually thin thickness and technical difficulties in making such parts - no experiments could be conducted to validate these optimizations.

In order to overcome the fragility that constrains further development of most of PZT devices, a new approach for the fabrication of a PZT-epoxy two phase device was achieved using sol-gel and spin coating techniques. A thin layer of 40% volume fraction PZT with epoxy matrix was deposited onto a dome-shape stainless steel layer from the pre-prepared mixture, and then post-baked for solidifying. Average 0.3 mm thick samples were fabricated and poled under various high voltages to enhance the piezoelectric properties. Surface examinations were carried out via AFM images. It was found that evaporation of air bubbles leaves deep holes on surface area, while surface tension pushes PZT particles together to form clusters. Clusters and holes together make a rather uneven surface. Piezoelectric coefficients d_{31}, d_{33} and the capacitance for three dome-shape samples were measured and plotted. d_{33} was found to increase as the poling voltage is increased, while d_{31} and capacitance do not show a clear tendency. Because the comparison was summarized on only three samples due to limited time, trends for d_{31} and capacitance were not fully studied.

5.2. Future Work

Though our PZT-epoxy samples increase the flexibility and are able to endure more force by introducing the epoxy matrix, reducing the high volume fraction of PZT does influence the electromechanical behavior of the samples.

Another approach inspired by McAlpine's work [4] can be applied directly as a novel method to print homogenous PZT ribbons, rather than composites or bulk materials, onto a flexible substrate for energy conversion. **Figure 5.1** gives the detailed process. A thin layer of photoresist ribbons is first applied onto a MgO substrate via spin coating, and developed after photolithography. Five hundred nanometers thick PZT layer is deposited onto the MgO substrate pre-patterned with photo resist, using RF-sputtering from a $Pb(Zr_{0.52}Ti_{0.48})O_3$ with 20% excess PbO. The extra PbO is used to compensate for the deficiency of Pb, due to the volatility of PbO. The remained photoresist will be subsequently stripped via light sonication in acetone. Phase transform is then performed at 750 ^{o}C to transfer PZT ribbons into the perovskite structure.

The main advantages of this novel design is that it allows the device to retain the high piezoelectric properties by making a homogeneous PZT device rather than a composites; while mechanical properties are enhanced due to the unique strip shape.

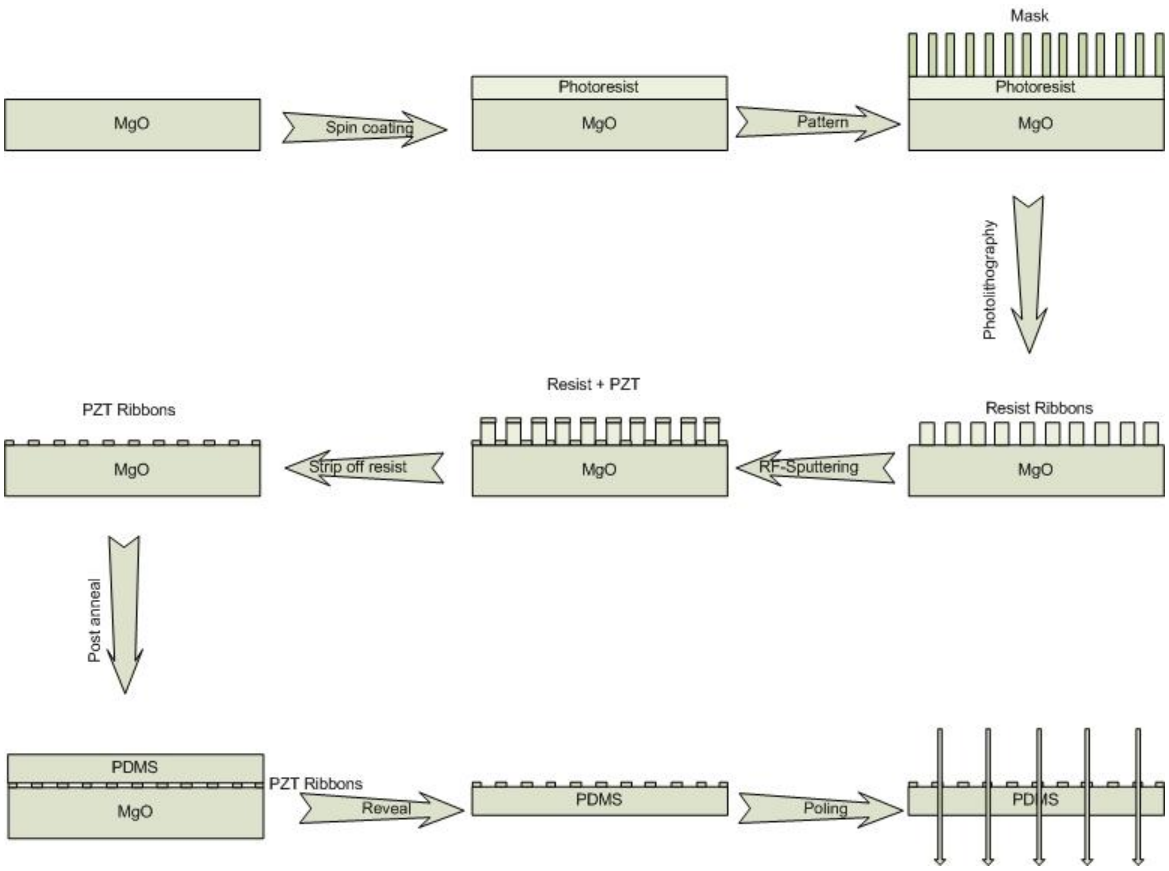

Figure 5.1 Process to print PZT ribbons onto PDMS for flexible energy conversion

The other focus of future work should be devoted to dome-shape sample fabrication experiment and modeling, and it includes these parts:

1. Sufficient dome-shape samples should be fabricated and poled at different poling voltages. A complete examination on trends of d_{31}, d_{33} and capacitance with increasing poling voltages can be conducted.

2. Multi-layer dome-shape devices are possible to make with spin coater.

3. Multi-phase samples with PZT-epoxy and other different scaled conductive materials may result in new properties.

References

[1] S. R. Anton and H. A. Sodano, "A review of power harvesting using piezoelectric materials (2003-2006)," *Smart Materials & Structures,* vol. 16, pp. R1-R21, Jun 2007.

[2] J. Baker, S. Roundy, and P. K. Wright, "Alternative Geometries for Increasing Power Density in Vibration Energy Scavenging for Wireless Sensor Networks," presented at the 3rd International Energy Conversion Engineering Conference, San Francisco, California, 2005.

[3] H. Gu, Y. Zhao, and M. L. Wang, "A wireless smart PVDF sensor for structural health monitoring," *Structural Control & Health Monitoring,* vol. 12, pp. 329-343, Jul-Dec 2005.

[4] Y. Qi, N. T. Jafferis, K. Lyons*, et al.*, "Piezoelectric Ribbons Printed onto Rubber for Flexible Energy Conversion," *Nano Letters,* vol. 10, pp. 524-528, Feb 2010.

[5] S. Roundy, "Energy Scavenging for Wireless Sensor Nodes with a Focus on Vibration-to-Electricity Conversion," Doctor of Philosophy, Engineering- Mechanical Engineering, University of California, Berkeley, Berkeley, 2003.

[6] S. Roundy, P. K. Wright, and J. M. Rabaey, *Energy Scavenging for Wireless Sensor Networks: with Special Focus on Vibrations* Kluwer Academic Publishers, 2004.

[7] Z. Y. Shen, W. Y. Shih, and W. H. Shih, "Mass detection sensitivity of piezoelectric cantilevers with a nonpiezoelectric extension," *Review of Scientific Instruments,* vol. 77, pp. -, Jun 2006.

[8] U. Soon-Chul, Y. Man-Soon, and H. Sung-Moo, "A newly designed chopper for pyroelectric infrared sensor by using a dome-shaped piezoelectric linear motor (DSPLM)," *Journal of Electroceramics,* vol. 23, pp. 242-247, Oct 2009.

[9] L. P. Wang, K. Deng, L. Zou*, et al.*, "Microelectromechanical systems (MEMS) accelerometers using lead zirconate titanate thick films," *Ieee Electron Device Letters,* vol. 23, pp. 182-184, Apr 2002.

[10] L. P. Wang, R. A. Wolf, Y. Wang*, et al.*, "Design, fabrication, and measurement of high-sensitivity piezoelectric microelectromechanical systems accelerometers," *Journal of Microelectromechanical Systems,* vol. 12, pp. 433-439, Aug 2003.

[11] C. H. Cheng and S. L. Tu, "Fabrication of a novel piezoelectric actuator with high load-bearing capability," *Sensors and Actuators a-Physical,* vol. 141, pp. 160-165, Jan 15 2008.

[12] J. Cheong, A. Goyal, S. A. Tadigadapa*, et al.*, "Fabrication and performance of a flextensional microactuator," *Journal of Micromechanics and Microengineering,* vol. 15, pp. 1947-1955, Oct 2005.

[13] O. Delas, A. Berry, P. Masson*, et al.*, "Optimizing the thickness of piezoceramic actuators for bending vibration of planar structures," *Journal of Intelligent Material Systems and Structures,* vol. 18, pp. 1191-1201, Nov 2007.

[14] N. S. Goo, S. C. Woo, and K. H. Park, "Influences of dome height and stored elastic energy on the actuating performance of a plate-type piezoelectric composite actuator," *Sensors and Actuators a-Physical,* vol. 137, pp. 110-119, Jun 12 2007.

[15] P. R, "Design, fabrication, test and evaluation of RF MEMS series switches using lead zirconate titanate (PZT) thin film actuators," Pennsylvania State University, 2007.

[16] K. S. S. Ram and S. K. Kiran, "Static behaviour of a laminated composite spherical shell cap with piezoelectric actuators," *Smart Materials & Structures,* vol. 17, pp. -, Jun 2008.

[17] H. Chandrahalim, S. A. Bhave, R. Polcawich*, et al.*, "Performance comparison of Pb(Zr(0.52)Ti(0.48))O(3)-only and Pb(Zr(0.52)Ti(0.48))O(3)-on-silicon resonators," *Applied Physics Letters,* vol. 93, Dec 8 2008.

[18] B. P. Otis and J. M. Rabaey, "A 300-mu W 1.9-GHz CMOS oscillator utilizing micromachined resonators," *Ieee Journal of Solid-State Circuits,* vol. 38, pp. 1271-1274, Jul 2003.

[19] K. S. V, "Compact FBAR filters offer low-loss performance," *Microw. RF,* vol. 30, pp. 127-36, 1991.

[20] K. M. Lakin, G. R. Kline, and K. T. Mccarron, "High-Q Microwave Acoustic Resonators and Filters," *Ieee Transactions on Microwave Theory and Techniques,* vol. 41, pp. 2139-2146, Dec 1993.

[21] S. K. Jiang X, Walker T, Portune A, Haber R, Geng X, Welter J and Hackenberger W S, "Single crystal piezoelectric composite transducers for ultrasound NDE applications," presented at the Proc. SPIE, 2008.

[22] G. H. Feng, "A piezoelectric dome-shaped-diaphragm transducer for microgenerator applications," *Smart Materials & Structures,* vol. 16, pp. 2636-2644, Dec 2007.

[23] G. H. Feng and E. S. Kim, "Piezoelectrically actuated dome-shaped diaphragm micropump," *Journal of Microelectromechanical Systems,* vol. 14, pp. 192-199, Apr 2005.

[24] G. H. Feng, C. C. Sharp, Q. F. Zhou*, et al.*, "Fabrication of MEMS ZnO domeshaped-diaphragm transducers for high-frequency ultrasonic imaging," *Journal of Micromechanics and Microengineering,* vol. 15, pp. 586-590, Mar 2005.

[25] A. Fleischman, R. Modi, A. Nair*, et al.*, "Miniature high frequency focused ultrasonic transducers for minimally invasive imaging procedures," *Sensors and Actuators a-Physical,* vol. 103, pp. 76-82, Jan 15 2003.

[26] K. M. Liang, H. Kunkel, C. Oakley*, et al.*, "Acoustic characterization of ultrasonic transducer materials: I. Blends of rigid and flexible epoxy resins used in piezocomposites," *Ultrasonics,* vol. 36, pp. 979-986, Oct 1998.

[27] K. M. Liang, C. Oakley, W. Huebner*, et al.*, "Acoustic characterization of ultrasonic transducer materials II. The effect of curing agent in binary epoxy blends on acoustic properties," *Ultrasonics,* vol. 37, pp. 201-207, Mar 1999.

[28] J. Peng, C. Chao, and H. Tang, "Piezoelectric micromachined ultrasonic transducer based on dome-shaped piezoelectric single layer," *Microsystem Technologies-Micro-and Nanosystems-*

Information Storage and Processing Systems, vol. 16, pp. 1771-1775, Oct 2010.

[29] D. P. Skinner, R. E. Newnham, and L. E. Cross, "Flexible composite transducers," *Materials Research Bulletin,* vol. 13, pp. 599-607, 1978.

[30] O. B. Wilson, United States. Naval Sea Systems Command., and United States. Naval Electronic Systems Command., *An introduction to the theory and design of sonar transducers*. Washington, D.C.: Naval Sea Systems Command : Naval Electronics Systems Command : For sale by the Supt. of Docs., U.S. G.P.O., 1985.

[31] Q. F. Zhou, Q. Q. Zhang, F. T. Djuth*, et al.*, "High frequency broadband PZT thick film ultrasonic transducers for medical imaging applications," *Ultrasonics,* vol. 44, pp. E711-E715, Dec 22 2006.

[32] A. Epifanov, "Theory of electron-avalanche ionization induced in solids by electromagnetic waves," *IEEE journal of quantum electronics,* vol. 17, pp. 2018-2022, 1981.

[33] V. Bedekar, J. Oliver, S. J. Zhang*, et al.*, "Comparative Study of Energy Harvesting from High Temperature Piezoelectric Single Crystals," *Japanese Journal of Applied Physics,* vol. 48, pp. -, Sep 2009.

[34] T. o. Ikeda, *Fundamentals of piezoelectricity*. Oxford ; New York: Oxford University Press, 1990.

[35] D. A. B. H. Jaffe, "Piezoelectric Transducer Materials," *Proc. IEEE,* vol. 53, pp. 1372-86, 1965.

[36] G. H. Haertling, "Ferroelectric ceramics: History and technology," *Journal of the American Ceramic Society,* vol. 82, pp. 797-818, Apr 1999.

[37] H. Maiwa, O. Kimura, K. Shoji*, et al.*, "Low temperature sintering of PZT ceramics without additives via an ordinary ceramic route," *Journal of the European Ceramic Society,* vol. 25, pp. 2383-2385, 2005.

[38] J. F. Fernandez, A. C. Caballero, P. Duran*, et al.*, "Improving sintering behaviour of BaTiO3 by small doping additions," *Journal of Materials Science,* vol. 31, pp. 975-981, Feb 15 1996.

[39] J. H. Kim and J. S. Park, "Coefficients of thermal expansion for single crystal piezoelectric fiber composites," *Composites Part B-Engineering,* vol. 38, pp. 795-799, 2007.

[40] F. F. Wang, C. J. He, Y. X. Tang*, et al.*, "Single-crystal 0.7Pb(Mg1/3Nb2/3)O-3-0.3PbTiO(3)/epoxy 1-3 piezoelectric composites prepared by the lamination technique," *Materials Chemistry and Physics,* vol. 105, pp. 273-277, Oct 15 2007.

[41] H. X. Wang, H. Q. Xu, T. H. He*, et al.*, "Electric properties of single-crystal PMN-31% PT epoxy 1-3 piezoelectric composites," *Physica Status Solidi a-Applications and Materials Science,* vol. 202, pp. 2829-2835, Nov 2005.

[42] R. E. Newnham and G. R. Ruschau, "Electromechanical Properties of Smart Materials," *Journal of Intelligent Material Systems and Structures,* vol. 4, pp. 289-294, 1993.

[43] R. E. Newnham, D. P. Skinner, and L. E. Cross, "Connectivity and piezoelectric-pyroelectric composites " *Materials Research Bulletin,* vol. 13, pp. 525-536, May 1978 1978.

[44] D. P. Skinner, R. E. Newnham, and L. E. Cross, "Connectivity and piezoelectric-pyroelectric

composites," *Material Research Bulletin,* vol. 13, pp. 599-607, 1978.

[45] S. M. Pilgrim and R. E. Newnham, "3-0 - A NEW COMPOSITE CONNECTIVITY," *Ieee Transactions on Ultrasonics Ferroelectrics and Frequency Control,* vol. 33, pp. 805-805, Nov 1986.

[46] C. J. Dias and D. K. DasGupta, "Inorganic ceramic/polymer ferroelectric composite electrets," *Ieee Transactions on Dielectrics and Electrical Insulation,* vol. 3, pp. 706-734, Oct 1996.

[47] K. Arlt and M. Wegener, "Piezoelectric PZT/PVDF-copolymer 0-3 Composites: Aspects on Film Preparation and Electrical Poling," *Ieee Transactions on Dielectrics and Electrical Insulation,* vol. 17, pp. 1178-1184, Aug 2010.

[48] S. Banerjee and K. A. Cook-Chennault, "Influence of Al Particle Size and PZT Volume Fraction on the Dielectric Properties of PZT-Epoxy-Aluminum Composites," 2011.

[49] T. Starner and J. A. Paradiso, "Human generated power for mobile electronics," *Low Power Electronics Design,* 2004.

[50] H. S. Yoon, G. Washington, and A. Danak, "Modeling, optimization, and design of efficient initially curved piezoceramic unimorphs for energy harvesting applications," *Journal of Intelligent Material Systems and Structures,* vol. 16, pp. 877-888, Oct 2005.

[51] S. Roundy, E. S. Leland, J. Baker*, et al.*, "Improving power output for vibration-based energy scavengers," *Ieee Pervasive Computing,* vol. 4, pp. 28-36, Jan-Mar 2005.

[52] M. L. Zhu, E. Worthington, and A. Tiwari, "Design Study of Piezoelectric Energy-Harvesting Devices for Generation of Higher Electrical Power Using a Coupled Piezoelectric-Circuit Finite Element Method," *Ieee Transactions on Ultrasonics Ferroelectrics and Frequency Control,* vol. 57, pp. 427-437, Feb 2010.

[53] J. H. Lin, X. M. Wu, T. L. Ren*, et al.*, "Modeling and simulation of piezoelectric MEMS energy harvesting device," *Integrated Ferroelectrics,* vol. 95, pp. 128-141, 2007.

[54] J. M. Dietl and E. Garcia, "Beam Shape Optimization for Power Harvesting," *Journal of Intelligent Material Systems and Structures,* vol. 21, pp. 633-646, Apr 2010.

[55] G.-H. Feng and E. S. Kim, "Universal concept for fabricating micron to millimeter sized 3-D parylene structures on rigid and flexible substrates " presented at the Micro Electro Mechanical Systems, 2003, Kyoto, 2003.

[56] S. Roundy and P. K. Wright, "A piezoelectric vibration based generator for wireless electronics," *Smart Materials & Structures,* vol. 13, pp. 1131-1142, Oct 2004.

[57] J. C. Stevens, J. C. Witt, B. E. Smith*, et al.*, "The frequency of carpal tunnel syndrome in computer users at a medical facility," *Neurology,* vol. 56, pp. 1568-1570, Jun 12 2001.

[58] M. Douwes, H. de Kraker, and B. M. Blatter, "Validity of two methods to assess computer use: Self-report by questionnaire and computer use software," *International Journal of Industrial Ergonomics,* vol. 37, pp. 425-431, May 2007.

[59] N. T. K. A. Cook-Chennault, M. A. Bitetto, "Piezoelectric Energy Harvesting: A Green and Clean

Alternative for Sustained Power Production," *Journal of Science and Technology: Special Issue on Sustainable Energy*.

[60] K. A. Cook-Chennault, N. Thambi, and A. M. Sastry, "Powering MEMS portable devices: a review of non-regenerative and regenerative power supply systems with special emphasis on piezoelectric energy harvesting systems," *Smart Materials & Structures,* vol. 17, 2008.

[61] T. Wacharasindhu and J. W. Kwon, "A micromachined energy harvester from a keyboard using combined electromagnetic and piezoelectric conversion," *Journal of Micromechanics and Microengineering,* vol. 18, Oct 2008.

[62] R. Reshmi, V. Natarajan, and M. K. Jayaraj, "Effect of Buffer Layer on the Properties of Laser Ablated PZT Thin Films," *Integrated Ferroelectrics,* vol. 117, pp. 104-109, 2010.

[63] K. A. Cook and A. M. Sastry, "An algorithm for selection and design of hybrid power supplies for MEMS with a case study of a micro-gas chromatograph system," *Journal of Power Sources,* vol. 140, pp. 181-202, Jan 2005.

[64] K. A. Cook, F. Albano, P. E. Nevius*, et al.*, "POWER (power optimization for wireless energy requirements): A MATLAB based algorithm for design of hybrid energy systems," *Journal of Power Sources,* vol. 159, pp. 758-780, Sep 2006.

[65] C. H. Nguyen, S. Pietrzko, and R. Buetikofer, "The influence of temperature and bonding thickness on the actuation of a cantilever beam by PZT patches," *Smart Materials & Structures,* vol. 13, pp. 851-860, Aug 2004.

[66] H. C. Gea, B. Zheng, and C. J. Chang, "Topology optimization of energy harvesting devices using piezoelectric materials," *Structural and Multidisciplinary Optimization,* vol. 38, pp. 17-23, Mar 2009.

[67] X. T. Gao, W. H. Shih, and W. Y. Shih, "Induced voltage of piezoelectric unimorph cantilevers of different nonpiezoelectric/piezoelectric length ratios," *Smart Materials & Structures,* vol. 18, pp. -, Dec 2009.

[68] G. Staines, H. Hofmann, J. Dommer*, et al.*, *Compact Piezo-Based High Voltage Generator - Part I: Quasi-Static Measurements* vol. 3, 2003.

[69] M. F, K. A, and C. R. B, "Power generation from piezoelectric lead zirconate titanate fiber composites," *Proc. Materials Research Symp,* p. p 736, 2003.

[70] D. P. S. a. L. E. C. R. E. Newnham, "Connectivity and Piezoelectric-pyroelectric Composites," 1978.

[71] A. Safari, A. Hall, and E. K. Akdogan, "Fatigue properties of piezoelectric-electrostrictive Pb(Mg-1/3,Nb-2/3)O-3-PbTiO3 monolithic bilayer composites," *Journal of Applied Physics,* vol. 100, Nov 1 2006.

[72] A. Safari, P. Ngernchuklin, E. K. Akdogan*, et al.*, "Electromechanical displacement of piezoelectric-electrostrictive monolithic bilayer composites," *Journal of Applied Physics,* vol. 105, Feb 1 2009.

[73] X. Shen, "Preparation and structure of rainbow piezoelectric ceramics," *Journal of Wuhan*

University of Technology-Materials Science Edition, vol. 18, pp. 24-26, Dec 2003.

[74] P. Ngernchuklin and A. Safari, "Bilayer Piezoelectric/Electrostrictive (P/E) Dome Unimorph," *Ieee Transactions on Ultrasonics Ferroelectrics and Frequency Control,* vol. 56, pp. 2744-2749, Dec 2009.

[75] X. P. Ruan, B. A. Cheeseman, A. Safari*, et al.*, "Design optimization of dome actuators," *Ieee Transactions on Ultrasonics Ferroelectrics and Frequency Control,* vol. 46, pp. 1489-1496, Nov 1999.

[76] R. C. Buchanan, E. Park, R. Surana*, et al.*, "High piezoelectric actuation response in graded Nd(2)O(3) and ZrO(2) doped BaTiO(3) structures," *Journal of Electroceramics,* vol. 26, pp. 116-121, Jun 2011.

[77] (2011, *Atomic Force Microscopy for Biological Applications Interactive Turoial*. Available: http://medicine.tamhsc.edu/basic-sciences/sbtm/afm/acknowledgements.php

Appendix A

Sample Preparation

1. Prepare a mixture of PZT and Epoxy

a) Volume fraction of PZT will be 40%. Specific amount of all components are listed in **Table 5-1**.

Volume= 4.5 cm^3 (ml)

Density of PZT = 7.55 g/cm^3

Volume fraction of PZT = 0.4

Table 5-1 Components and amount for PZT-epoxy mixture

PZT (gm)	13.59
DGEBA (ml)	2.7
DGEBA Hardener (ml)	0.36

(The table reflects the volume and weights of components for preparing a sample of volume 4.5 cm^3 (ml). Adjustments should be made if a sample of larger volume is to be prepared. Powders will be measured by scale, Epoxy and hardener will be measured by micropipette)

b) Take the amount of PZT powder listed in Table1, measured in a weighing scale;

c) After that, they are dispersed in 2.5 ml ethanol (as solvent) in a beaker;

d) Then add the certain amount of epoxy mentioned in Table 1 into mixture by micropipette, stir them in a sonicator for 15 min.

e) After that, Epoxy Hardener is applied: hand mix for 15 min on the hotplate at 75C then the ethanol is allowed to evaporate and the mixture becomes pasty.

2. Sample fabrication by Spin Coating Route

f) Prepare one circular shape Stainless steel foil, with diameter slightly larger than 1.0 inch. Press them in mold to pre-make it a smooth dome-shape.

g) Apply mixture onto dome-shape stainless steel by using a steel stick (Do NOT use syringe, epoxy will get stuck in it and it's hard to clean) and then place it onto central shaft of spinner

h) Spin at 500 rpm for 5 s and then at 800 rpm for 40s

i) Take the foil out, put on the hot plate with 75C and cure for 3min. Then repeat g) to h) for several times.

j) Cure sample on hot plate with 75C for at least 6 hours.

k) Measure thickness of sample by digital caliper. Measure five times and take the average.

3. Device Poling

l) Put sample in the mold.

m) An isothermal bath filled with silicone oil is set at a temperature of 80 Celsius degree

n) Then place the mold with sample inside the high voltage setup developed and immerse the setup in the silicone bath with the help of tweezers.

o) Plug in the high voltage power supply unit to the 220 vac supply and connect the output cable and the ground cable to the sample.

p) After all the connections (recheck) are completed, turn on the power for the high voltage equipment and turn the dial for the high voltage to X kV/mm. Depend on the measurement results from 2.(k), the voltage will be X kV/mm*Thickness.

q) After 30 minutes turn the high voltage dial to 0 kV and then turn off the switch and the power for the high voltage equipment. Turn off the 220 vac power supply and then remove the plug for the high voltage equipment and remove the output cables from the sample.

r) Remove the sample from the hot silicone bath and cool it to room temperature.